



CHORUS

This is the accepted manuscript made available via CHORUS. The article has been published as:

Twisted chimera states and multicore spiral chimera states on a two-dimensional torus

Jianbo Xie, Edgar Knobloch, and Hsien-Ching Kao

Phys. Rev. E **92**, 042921 — Published 26 October 2015

DOI: [10.1103/PhysRevE.92.042921](https://doi.org/10.1103/PhysRevE.92.042921)

Twisted chimera states and multi-core spiral chimera states on a two-dimensional torus

Jianbo Xie* and Edgar Knobloch†

Department of Physics, University of California at Berkeley, Berkeley CA 94720, USA

Hsien-Ching Kao‡

Wolfram Research Inc., Champaign, IL 61820, USA

Chimera states consisting of domains of coherently and incoherently oscillating oscillators in a two-dimensional periodic array of nonlocally-coupled phase oscillators are studied. In addition to the one-dimensional chimera states familiar from one spatial dimension, two-dimensional structures termed twisted chimera states and spiral wave chimera states are identified in simulations. The properties of many of these states, including stability, are determined using an evolution equation for a complex order parameter, and are found to be in agreement with the simulations.

PACS numbers: 05.45.a, 89.75.Kd

* swordwave@berkeley.edu

† knobloch@berkeley.edu

‡ hkao@wolfram.com

I. INTRODUCTION

Chimera states are states of partial synchronization in which a group of oscillators oscillate in phase while the remaining oscillators oscillate incoherently [1–3]. States of this type were first identified in systems of phase oscillators with nonlocal coupling [1] and a fairly detailed understanding of the origin of such states in one spatial dimension and their stability properties has now been achieved [4, 5]. Chimera states may be stationary or they may travel [5, 6]. A system may exhibit a single coherent cluster or multiple coherent clusters; the latter may be equally or unequally distributed [5, 6]. Although first discovered in numerical simulations, a self-consistency analysis based on the Ott-Antonsen Ansatz [4, 7, 8] has provided valuable information about the splitting or coalescence of chimera states as parameters are varied; this approach allows in addition the determination of the stability of such states and hence provides a first step towards understanding the types of bifurcations that chimera states may undergo [4, 5].

Rather less is known about chimera states in two-dimensional oscillator arrays and existing results are largely based on numerical simulations [9–11]. Both two- [9–11] and three-dimensional [12] arrays have been studied and the results have revealed new types of chimera states, in addition to the counterparts of the one-dimensional states already mentioned. In two dimensions these include spiral chimera states with an incoherent core while the oscillators outside the core oscillate coherently [11, 13]. In this paper we consider the case of two-dimensional oscillator arrays with nonlocal coupling, with a view to studying, both numerically and analytically, different states of partial synchrony in two dimensions. Like earlier work, our work is restricted to arrays of phase-coupled oscillators with periodic boundary conditions in both directions, i.e., to phase oscillators on a (flat) torus.

First steps in this direction were taken by Kim *et al.* [14] in their study of the system

$$\frac{d\theta_{ij}}{dt} = \omega - \frac{K}{N(R)} \sum_{(m-i)^2 + (n-j)^2 \leq R^2} \sin(\theta_{ij} - \theta_{mn} + \alpha). \quad (1)$$

Here θ_{ij} denotes the phase of the oscillator at position (i, j) on a two-dimensional periodic lattice, K is the coupling strength, and $N(R)$ is the number of oscillators whose distance to (i, j) is no larger than R . They found and investigated many of the interesting patterns that arise as α varies in the range $[-\pi, \pi]$, but did not observe chimera states. In 2012, Hagerstrom *et al.* created a physical realization of a two-dimensional iterated map with nonlocal coupling and periodic boundary conditions, and observed chimera states in an experiment [15]. Meanwhile, Omel’chenko *et al.* [11] presented a series of numerical experiments on the same system as used in [14] but with a careful preparation of initial conditions. They reported chimera states of three types: a coherent spot, an incoherent spot, and different stripe patterns. In addition, they observed a stable configuration of four spirals. This work has recently been extended to three dimensions [12]. While the results in these papers are largely based on numerical simulations, Panaggio and Abrams used asymptotic methods to derive conditions under which two-dimensional “spot” and “stripe” chimeras can exist on a two-dimensional periodic domain [16]. With their method, they also reveal an asymmetric chimera state; however, this state is unstable and appears in simulations only as a

transient. In the work reported below additional two-dimensional chimera states, including states we call twisted chimera states and multi-core spiral wave chimera states, are observed and studied.

The system we consider consists of an oscillator array on a two-dimensional torus. The continuous version of the model leads to the following evolution equation for the phase $\theta(x, y, t)$:

$$\frac{\partial \theta(x, y, t)}{\partial t} = - \int_{-\pi}^{\pi} \int_{-\pi}^{\pi} G(x - x', y - y') \sin(\theta(x, y, t) - \theta(x', y', t) + \alpha) dx' dy'. \quad (2)$$

To make the system analytically tractable, we assume the coupling kernel G can be decomposed as $G(x, y) = G_x(x) + G_y(y)$, where G_x and G_y are functions representing the coupling in the x and y directions, respectively. Inspired by the work in [5], we choose G_x and G_y from the following two families:

$$G_n^{(1)}(x) \equiv \cos(nx), \quad G_n^{(2)}(x) \equiv \cos(nx) + \cos[(n + 1)x].$$

With these coupling kernels, we observe chimera states on a two-dimensional torus with random initial conditions, including twisted chimeras and a variety of spiral wave chimeras. The simulations are carried out using a fourth-order Runge-Kutta method with time step $\delta t = 0.025$. Both x and y directions are discretized into N uniform intervals with $N = 256$ or $N = 512$.

This paper is organized as follows. In Section II we introduce the effective order parameter equation we will use to describe the phase patterns obtained in numerical simulations. These are described in Sections III and IV for two different choices of the coupling kernel $G(x, y)$. These sections also relate the simulations to solutions of the order parameter equation and use the latter to determine the stability properties of the different states found. The paper ends with a brief discussion in Section V.

II. EFFECTIVE EQUATION

As in the one-dimensional case, an equivalent description of Eq. (2) can be obtained by constructing an equation for the local spatial average $z(x, y, t)$ of $\exp[i\theta(x, y, t)]$ defined by

$$z(x, y, t) \equiv \lim_{\delta \rightarrow 0^+} \frac{1}{\delta^2} \int_{-\delta/2}^{\delta/2} \int_{-\delta/2}^{\delta/2} \exp[i\theta(x + x', y + y', t)] dx' dy'. \quad (3)$$

The evolution equation for z then takes the form [17]

$$z_t = \frac{1}{2} (\exp(-i\alpha)Z - \exp(i\alpha)z^2 Z^*), \quad (4)$$

where $Z(x, y, t) \equiv K[z](x, y, t)$ and K is a compact linear operator defined via the relation

$$K[u](x, y, t) \equiv \int_{-\pi}^{\pi} \int_{-\pi}^{\pi} G(x - x', y - y') u(x', y', t) dx' dy'. \quad (5)$$

A derivation of Eq. (4) based on the Ott–Antonsen ansatz is very similar to the one-dimensional case [5, 18] and is omitted.

Stationary rotating solutions of Eq. (4) take the form

$$z(x, y, t) = \tilde{z}(x, y) \exp(-i\Omega t), \quad (6)$$

where Ω satisfies the nonlinear-nonlocal eigenvalue problem

$$i\Omega\tilde{z} + \frac{1}{2} \left[\exp(-i\alpha)\tilde{Z}(x, y) - \tilde{z}^2 \exp(i\alpha)\tilde{Z}^*(x, y) \right] = 0. \quad (7)$$

Here $\tilde{z}(x, y)$ describes the spatial profile of the rotating solution and

$$\tilde{Z}(x, y) \equiv K[\tilde{z}](x, y) = R(x, y) \exp(i\Theta(x, y)) \quad (8)$$

is the (complex) local order parameter; this parameter has magnitude $R(x, y)$ and phase $\Theta(x, y)$.

Solving Eq. (7) as a quadratic equation in \tilde{z} we obtain

$$\tilde{z}(x, y) = \exp(i\beta) \frac{\Omega - \mu(x, y)}{\tilde{Z}^*(x, y)} = \frac{\exp(i\beta)\tilde{Z}(x, y)}{\Omega + \mu(x, y)}, \quad (9)$$

where $\beta \equiv (\pi/2) - \alpha$, and $\mu(x, y)$ equals $[\Omega^2 - |\tilde{Z}(x, y)|^2]^{1/2}$ when $|\Omega| > |\tilde{Z}(x, y)|$ and $i[|\tilde{Z}(x, y)|^2 - \Omega^2]^{1/2}$ when $|\Omega| < |\tilde{Z}(x, y)|$ for reasons explained in [17]. Combining this equation and the relation between \tilde{z} and \tilde{Z} gives us the self-consistency equation

$$R(x, y) \exp(i\Theta(x, y)) = \exp(i\beta) \int_{-\pi}^{\pi} \int_{-\pi}^{\pi} G(x - x', y - y') \exp(i\Theta(x', y')) h(x', y') dx' dy', \quad (10)$$

where

$$h(x, y) \equiv \frac{\Omega - \sqrt{\Omega^2 - R^2(x, y)}}{R(x, y)}. \quad (11)$$

As in the one-dimensional case, temporal stability of the stationary rotating solution is determined by the spectrum of the following linear operator:

$$v_t = L[v] \equiv i\mu(x, y)v + \frac{1}{2} \left[\exp(-i\alpha)V(x, y, t) - \exp(i\alpha)\tilde{z}^2 V^*(x, y, t) \right], \quad (12)$$

where $V(x, y, t) \equiv K[v]$.

In the following we perform numerical simulations with N^2 identical oscillators and use the results to determine the order parameter amplitude and phase by discretizing the definition

$$R(x, y) \exp(i\Theta(x, y)) = \int G(x - x', y - y') \exp(i\theta(x', y')) dx' dy' \quad (13)$$

as follows:

$$R_{nm} \exp(i\Theta_{nm}) = \left(\frac{2\pi}{N} \right)^2 \sum_{n', m'} G \left(\frac{2(n - n')\pi}{N}, \frac{2(m - m')\pi}{N} \right) \exp(i\theta_{n'm'}). \quad (14)$$

Here θ_{nm} is the phase of the oscillator at site (n, m) , and R_{nm} and Θ_{nm} are the modulus and phase of the expression on the right. We use the results to establish the symmetry properties of the order parameter and to suggest the form of the solution of the self-consistency relation (10).

III. THE CASE $G_x = G_y = G_n^{(1)}$

We consider first the case where $G_x = \cos(nx)$ and $G_y = \cos(ny)$. In [5] we discussed the one-dimensional system with $G(x) = \cos(nx)$, where splay states and $2n$ -cluster chimera states are observed. In the current two-dimensional system, counterparts of the splay states are still present, although no counterparts of $2n$ -cluster chimera states were observed: $2n$ -cluster chimera states are always unstable in two dimensions. This is because the 2-cluster state is unstable (Sec. III B) and the stability calculation for the case $n > 1$ is the same. However, in addition to the stable splay states, we have also observed two new types of chimera states. One is the twisted chimera state already mentioned, in which a coherent stripe with uniformly varying phase distribution coexists with an incoherent domain, while the other is a multi-core spiral wave chimera. These states are described below.

Before proceeding we wish to point out two facts about Eq. (2) with the present coupling. First, the system is invariant under the three reflections $(x, y) \rightarrow (-x, y)$, $(x, y) \rightarrow (x, -y)$, and $(x, y) \rightarrow (y, x)$, i.e., it is invariant under the group D_4 of rotations and reflections of a square. It follows that if $\theta(x, y, t)$ is a solution, then so are $\theta(-x, y, t)$, $\theta(x, -y, t)$, and $\theta(y, x, t)$. Second, if $\int_{-\pi}^{\pi} G_y(y) dy = 0$, then the following statement holds: if $\theta_1(x, t)$ is a solution for the one-dimensional system

$$\frac{\partial \theta(x, t)}{\partial t} = - \int_{-\pi}^{\pi} G(x - x') \sin[\theta(x, t) - \theta(x', t) + \alpha] dx', \quad (15)$$

then $\theta_2(x, y, t) \equiv \theta_1(x, 2\pi t)$ is a solution of Eq. (2). We say that the solution θ_2 of the two-dimensional system is inherited from the solution θ_1 for the corresponding one-dimensional system.

A. Splay states

Splay states with a phase that varies uniformly with respect to x are observed in one-dimensional systems. The inherited solution of the two-dimensional system is also observed in numerical simulations. Figure 1 shows two examples in which the phase varies uniformly in the x direction. Solutions in which the phase varies uniformly in the y direction are also observed (not shown).

The splay state in Fig. 1 can be written in the form

$$\theta(x, y, t) = -\Omega t + qx, \quad (16)$$

where $-\Omega$ represents the overall rotation frequency and q (an integer) is the twist number. Substituting Eq. (16) into Eq. (2) we obtain a relation for the rotation frequency:

$$\Omega = \int_{-\pi}^{\pi} \int_{-\pi}^{\pi} G(x, y) \sin(qx + \alpha) dx dy. \quad (17)$$

As in the one-dimensional case, states of this type travel with speed $c = \Omega/q$, i.e., to the right when both Ω and q have the same sign and to the left when Ω and q have opposite signs.

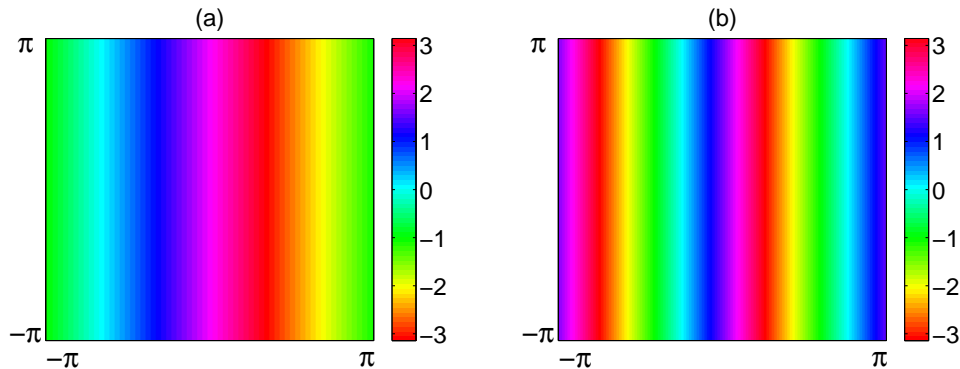


FIG. 1. (Color online) Snapshot of the phase pattern for splay states in two dimensions. (a) The phase distribution $\theta(x, y, t)$ for $G_x = \cos(x)$, $G_y = \cos(y)$. (b) The phase distribution $\theta(x, y, t)$ for $G_x = \cos(x) + \cos(2x)$, $G_y = \cos(y) + \cos(2y)$. The simulations are done with $\beta = 0.05$, $N = 256$ from a random initial condition. Colors indicate the phase of the oscillators.

To investigate the linear stability of the splay states, we use the approach of [5] and suppose that $\theta(x, y, t)$ is perturbed by $\epsilon \exp[\lambda t + i(k_x x + k_y y)]$ with $0 < \epsilon \ll 1$. A straightforward calculation, using the fact that G_x, G_y are both even and $\hat{G}_{y0} = 0$, leads to the following relation for the growth rate λ of the perturbation:

$$\lambda = \frac{1}{2} \left[\exp(i\alpha) (\hat{G}_{x, q-k_x} \delta_{k_y, 0} + \delta_{k_x, q} \hat{G}_{y, -k_y}) + \exp(-i\alpha) (\hat{G}_{x, -k_x-q} \delta_{k_y, 0} + \delta_{k_x, -q} \hat{G}_{y, -k_y}) \right] - \hat{G}_{x, q} \cos \alpha, \quad (18)$$

where $\hat{G}_{x, k} \equiv \int_{-\pi}^{\pi} G_x(x) \exp(ikx) dx$ etc. This relation shows that when $0 < \alpha < \pi/2$, the splay state is linearly stable when $|q| = n$ if $G_x = G_y = G_n^{(1)}$ and $|q| = n$ or $n+1$ if $G_x = G_y = G_n^{(2)}$.

B. Two-cluster chimera states

As in one dimension the splay states may coexist with stable chimera states. However, no stable analogues of the $2n$ -cluster chimera states familiar from the one-dimensional problem have been observed in two dimensions since such states are now unstable. To demonstrate this we first compute such states using the self-consistency analysis and then determine their stability properties.

In view of the coupling kernel $G(x, y)$ the local order parameter must take the form $\tilde{Z}(x, y) = R_0 \cos(nx)$ (modulo translations), a result expected to be exact in the limit $N \rightarrow \infty$. The self-consistency relation for R_0 is

$$R_0^2 = \exp(i\beta) \left\langle \Omega - \sqrt{\Omega^2 - R_0^2 \cos^2(nx)} \right\rangle. \quad (19)$$

Here the bracket $\langle \cdot \rangle$ is defined by $\langle f \rangle = \int_{-\pi}^{\pi} \int_{-\pi}^{\pi} f(x', y') dx' dy'$. Thus the self-consistency equation for R_0 has the same form as in one dimension (1D) except that the bracket represents an integral over a torus rather than a ring. Therefore, if Ω' and R_0' is the solution

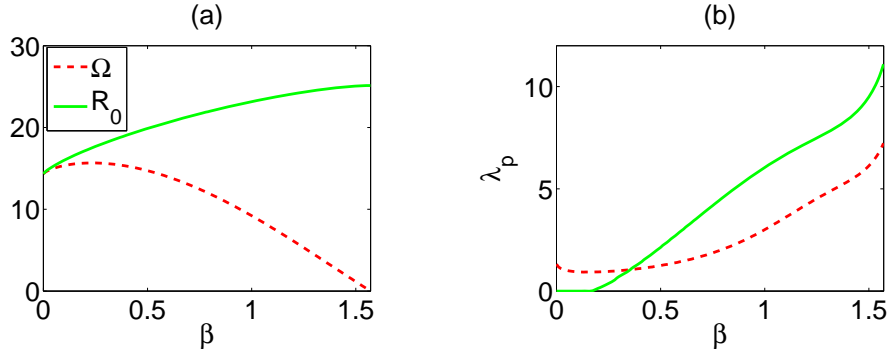


FIG. 2. (Color online) Dependence of (a) R_0 and Ω , and (b) the point eigenvalues λ_p on the parameter β .

for 1D case, then $\Omega = 2\pi\Omega'$ and $R_0 = 2\pi R'_0$ is the solution in two dimensions (2D). The solution of Eq. (19) is shown in Fig. 2(a). Since the right side of Eq. (19) is identical for all $n = k/2$, $k \in \mathbb{N}$, it follows that the same solution describes all $2n$ -cluster chimera states, $n = 1, 2, \dots$

The linear stability of the $2n$ -cluster chimera states determined by the above analysis can be studied using Eq. (12). This equation is solved by

$$v(x, y, t) = \exp(\lambda t)v_1(x, y) + \exp(\lambda^* t)v_2^*(x, y), \quad (20)$$

leading to the eigenvalue problem

$$\lambda \begin{pmatrix} v_1 \\ v_2 \end{pmatrix} = \frac{1}{2} \begin{pmatrix} 2i\mu + \exp(-i\alpha)K & -\exp(i\alpha)\tilde{z}^2 K \\ -\exp(-i\alpha)\tilde{z}^{*2} K & -2i\mu^* + \exp(i\alpha)K \end{pmatrix} \begin{pmatrix} v_1 \\ v_2 \end{pmatrix}. \quad (21)$$

Since the operator K is compact, its spectrum consists of two parts, a continuous spectrum given by $\{i\mu(x, y), -i\mu^*(x, y)\}$ with $x, y \in [-\pi, \pi]$ and a (possibly empty) point spectrum. The spectrum is in addition symmetric with respect to the real axis: if λ is an eigenvalue with eigenvector $(v_1, v_2)^T$, then λ^* is an eigenvalue with eigenvector $(v_2^*, v_1^*)^T$. The continuous spectrum is stable (negative) or neutrally stable (purely imaginary). Thus the stability of the chimera states is solely determined by the point spectrum. In the following we use the term *stable* to indicate absence of (exponentially growing) instability.

We can compute unstable point eigenvalues λ_p numerically. For this purpose we rewrite Eq. (21) in the form

$$\mathbf{L}\mathbf{v} \equiv \begin{pmatrix} 2 - \frac{\exp(-i\alpha)K}{\lambda_p - i\mu} & \frac{\exp(i\alpha)\tilde{z}^2 K}{\lambda_p - i\mu} \\ \frac{\exp(-i\alpha)\tilde{z}^{*2} K}{\lambda_p + i\mu^*} & 2 - \frac{\exp(i\alpha)K}{\lambda_p + i\mu^*} \end{pmatrix} \begin{pmatrix} v_1 \\ v_2 \end{pmatrix} = 0, \quad (22)$$

and define $f \equiv \frac{1}{4} \frac{\exp(-i\alpha)}{\lambda_p - i\mu}$, $f^c \equiv \frac{1}{4} \frac{\exp(i\alpha)}{\lambda_p + i\mu^*}$, $g \equiv \frac{1}{4} \frac{\exp(i\alpha)\tilde{z}^2}{\lambda_p - i\mu}$, and $g^c \equiv \frac{1}{4} \frac{\exp(-i\alpha)\tilde{z}^{*2}}{\lambda_p + i\mu^*}$. Note that f^c is the complex conjugate of f only when λ_p is real, and likewise for g^c . Since the lack of smoothness of \tilde{Z} can lead to significant numerical error when the above problem is solved

directly using a global collocation method, we employ instead Fourier basis functions. These are particularly convenient in view of the sinusoidal coupling kernel [4, 5]. Following the convention used in [5], we write

$$\mathbf{v} = \frac{1}{4\pi^2} \sum_{m,n} \hat{\mathbf{v}}_{mn} \exp(-imx) \exp(-iny). \quad (23)$$

In this basis, Eq. (22) takes the form

$$\sum_{m,n} \mathbf{B}_{kl,mn} \hat{\mathbf{v}}_{mn} = 0, \quad (24)$$

where $\hat{\mathbf{v}}_{mn} = (\hat{v}_{1,mn}, \hat{v}_{2,mn})$,

$$\mathbf{B}_{kl,mn} = \begin{pmatrix} 2\pi^2 \delta_{k,m} \delta_{l,n} - \hat{f}_{k-m} \hat{g}_{l-n} \hat{G}_{mn} & \hat{g}_{k-m} \hat{g}_{l-n} \hat{G}_{mn} \\ \hat{g}_{k-m} \hat{g}_{l-n} \hat{G}_{mn} & 2\pi^2 \delta_{k,m} \delta_{l,n} - \hat{f}_{k-m} \hat{f}_{l-n} \hat{G}_{mn} \end{pmatrix},$$

and \hat{f}_l , \hat{f}_l^c , \hat{g}_l , \hat{g}_l^c are the Fourier coefficients of f , f^c , g and g^c , respectively; the latter are defined by $\hat{f}_{kl} = \langle f \exp(ikx) \exp(ily) \rangle$, etc.

The point eigenvalue λ_p satisfies the condition $\det \mathbf{B}(\lambda_p) = 0$. We use $n = 1$ as an example. In this case $\hat{G}_{mn} = 2\pi^2$ whenever $(m, n) = (\pm 1, 0)$ and $(0, \pm 1)$, and 0 otherwise. Therefore, λ_p satisfies

$$\det \begin{pmatrix} 1 - \hat{f}_{0,0} & \hat{g}_{0,0} & -\hat{f}_{-2,0} & \hat{g}_{-2,0} & -\hat{f}_{-1,1} & \hat{g}_{-1,1} & -\hat{f}_{-1,-1} & \hat{g}_{-1,-1} \\ \hat{g}_{0,0}^c & 1 - \hat{f}_{0,0}^c & \hat{g}_{-2,0}^c & -\hat{f}_{-2,0}^c & \hat{g}_{-1,1}^c & -\hat{f}_{-1,1}^c & \hat{g}_{-1,-1}^c & -\hat{f}_{-1,-1}^c \\ -\hat{f}_{2,0} & \hat{g}_{2,0} & 1 - \hat{f}_{0,0} & \hat{g}_{0,0} & -\hat{f}_{1,1} & \hat{g}_{1,1} & -\hat{f}_{1,-1} & \hat{g}_{1,-1} \\ \hat{g}_{2,0}^c & -\hat{f}_{2,0}^c & \hat{g}_{0,0}^c & 1 - \hat{f}_{0,0}^c & \hat{g}_{1,1}^c & -\hat{f}_{1,1}^c & \hat{g}_{1,-1}^c & -\hat{f}_{1,-1}^c \\ -\hat{f}_{1,-1} & \hat{g}_{1,-1} & -\hat{f}_{-1,-1} & \hat{g}_{-1,-1} & 1 - \hat{f}_{0,0} & \hat{g}_{0,0} & -\hat{f}_{0,-2} & \hat{g}_{0,-2} \\ \hat{g}_{1,-1}^c & -\hat{f}_{1,-1}^c & \hat{g}_{-1,-1}^c & -\hat{f}_{-1,-1}^c & \hat{g}_{0,0}^c & 1 - \hat{f}_{0,0}^c & \hat{g}_{0,-2}^c & -\hat{f}_{0,-2}^c \\ -\hat{f}_{1,1} & \hat{g}_{1,1} & -\hat{f}_{-1,1} & \hat{g}_{-1,1} & -\hat{f}_{0,2} & \hat{g}_{0,2} & 1 - \hat{f}_{0,0} & \hat{g}_{0,0} \\ \hat{g}_{1,1}^c & -\hat{f}_{1,1}^c & \hat{g}_{-1,1}^c & -\hat{f}_{-1,1}^c & \hat{g}_{0,2}^c & -\hat{f}_{0,2}^c & \hat{g}_{0,0}^c & 1 - \hat{f}_{0,0}^c \end{pmatrix} = 0. \quad (25)$$

This equation applies for the coupling kernels $G_x = G_y = G_1^{(1)}$ and will be used in later sections. For 2-cluster chimera states we have in addition $\hat{f}_{kl} = \hat{g}_{kl} = \hat{f}_{kl}^c = \hat{g}_{kl}^c = 0$ whenever $l \neq 0$. Thus Eq. (25) reduces to

$$\det \begin{pmatrix} 1 - \hat{f}_{0,0} & \hat{g}_{0,0} & -\hat{f}_{-2,0} & \hat{g}_{-2,0} \\ \hat{g}_{0,0}^c & 1 - \hat{f}_{0,0}^c & \hat{g}_{-2,0}^c & -\hat{f}_{-2,0}^c \\ -\hat{f}_{2,0} & \hat{g}_{2,0} & 1 - \hat{f}_{0,0} & \hat{g}_{0,0} \\ \hat{g}_{2,0}^c & -\hat{f}_{2,0}^c & \hat{g}_{0,0}^c & 1 - \hat{f}_{0,0}^c \end{pmatrix} = 0, \quad (26)$$

and two copies of the block

$$\det \begin{pmatrix} 1 - \hat{f}_{0,0} & \hat{g}_{0,0} \\ \hat{g}_{0,0}^c & 1 - \hat{f}_{0,0}^c \end{pmatrix} = 0. \quad (27)$$

One branch of the point spectrum comes from Eq. (26). The resulting point eigenvalue λ_p is computed using continuation based on Newton's method and is shown in Fig. 2(b) (green solid line). Notice that

$$\hat{f}_{0,0} = \frac{1}{4} \left\langle \frac{\exp(-i\alpha)}{\lambda_p - i\sqrt{\Omega^2 - R_0^2 \cos^2 x}} \right\rangle = \frac{1}{4} \int_{-\pi}^{\pi} \frac{\exp(-i\alpha)}{\lambda_p/(2\pi) - i\sqrt{\Omega^2 - R_0^2 \cos^2 x}} dx. \quad (28)$$

From this and similar relations we conclude that if λ'_p is an eigenvalue in 1D, then $\lambda_p = 2\pi\lambda'_p$ is an eigenvalue in 2D. A second branch of the point spectrum comes from Eq. (27) and is also shown in Fig. 2(b) (red dashed line). This point eigenvalue has double multiplicity because the factor (27) occurs twice; the figure shows that it is positive for all $0 \leq \beta \leq \frac{\pi}{2}$, thereby explaining why we were unable to find $2n$ -cluster chimera states starting from random initial conditions.

C. Twisted chimera states

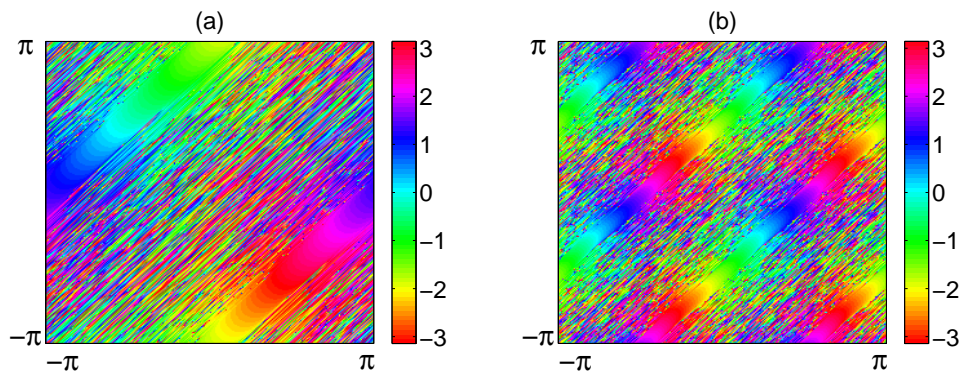


FIG. 3. (Color online) Snapshots of the phase patterns for twisted chimera states. (a) The phase distribution $\theta(x, y, t)$ for $G_x = G_y = G_1^{(1)}$. (b) The phase distribution $\theta(x, y, t)$ for $G_x = G_y = G_2^{(1)}$. The simulations are done with $\beta = 0.05$, $N = 256$ and random initial condition. Colors indicate the phase of the oscillators.

As mentioned above, twisted chimera states are obtained in numerical simulations with the coupling kernels $G_x = \cos(nx)$, $G_y = \cos(ny)$. Figure 3 provides examples for $n = 1, 2$ and $\beta = 0.05$. In these states the coherent clusters form closed stripes on a torus. In addition, the phase varies uniformly along the stripes. We use the term twist number to indicate the number of times the stripe wraps in either the x or the y direction. Thus the states in Figs. 3(a,b) correspond to 1:1 and 2:2 twisted chimeras, respectively. Numerical simulations suggest that this type of chimera state is one of the two most frequently observed states (the other being a splay state) when starting from random initial conditions with $\beta \lesssim 0.12$.

To understand the properties of the twisted chimera states we invoke the self-consistency equation (10). Figures 4(a,b) show the pattern of $R(x, y)$ and $\Theta(x, y)$ for the 1:1 twisted

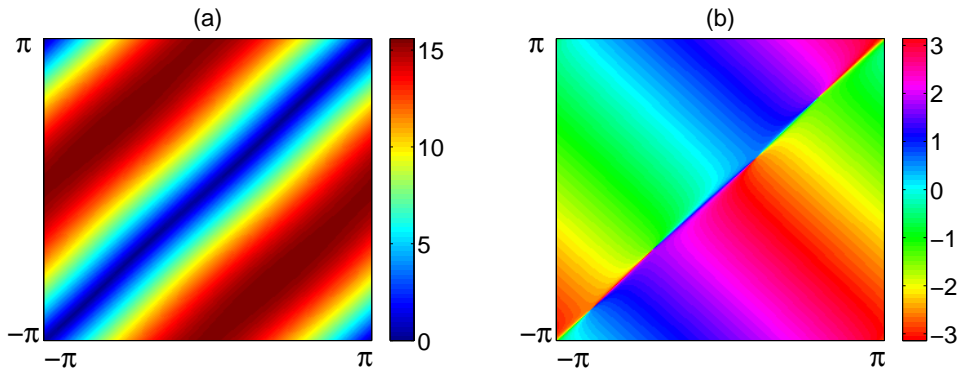


FIG. 4. The (real) order parameters (a) $R(x, y)$, and (b) $\Theta(x, y)$ for the 1:1 twisted chimera state shown in Fig. 3(a). In panel (a), the color indicates the amplitude of the local order parameter $R(x, y)$. In (b), the color indicates the phase.

chimera state obtained from the numerical simulation reported in Fig. 3(a). To understand the properties of these empirical order parameter fields we need to solve Eq. (10) for $R(x, y)$ and $\Theta(x, y)$. This formidable task can be simplified using appropriate symmetry relations valid for our choice of G_x and G_y . We illustrate the procedure in Appendix A in the case $n = 1$, obtaining $R \exp(i\Theta) = \frac{R_0}{2} (\exp(ix) - \exp(iy))$. It follows that the self-consistency requirement takes the form

$$R_0^2 = \exp(i\beta) \left\langle \Omega - \sqrt{\Omega^2 - R_0^2 \sin^2 \left(\frac{x-y}{2} \right)} \right\rangle. \quad (29)$$

The detailed derivation of this expression can also be found in Appendix A.

Equation (29) is identical to Eq. (19) with a change of coordinates $u \equiv x + y$, $v \equiv \frac{x-y}{2}$. Thus the dependence of Ω and R_0 on β is identical to that shown in Fig. 2(a). When $\beta = 0$, $\Omega = R_0 \approx 14.346$, which is consistent with the value $\Omega = R_0 = 4\pi^2 - 8\pi$ obtained analytically from Eq. (29). As in the 1D case, the boundary between coherent and incoherent domains is determined by the relation $\Omega = R_0 |\sin(\frac{x-y}{2})|$, implying that the coherent fraction (by area) is given by $r = 1 - 2\pi^{-1} \sin^{-1}(\Omega/R_0)$. The dependence of r on β is shown in Fig. 5(a).

The stability of the twisted chimera states can be analyzed in the same way as done for the $2n$ -cluster chimera states. When $n = 1$, λ_p is still determined by Eq. (25). It turns out that many elements in Eq. (25) vanish and the equation for the point eigenvalue λ_p reduces to the three conditions

$$\det \begin{pmatrix} 1 - \hat{f}_{0,0} & -\hat{f}_{-1,1} & \hat{g}_{-2,0} & \hat{g}_{-1,-1} \\ -\hat{f}_{1,-1} & 1 - \hat{f}_{0,0} & \hat{g}_{-1,-1} & \hat{g}_{0,-2} \\ \hat{g}_{2,0}^c & \hat{g}_{1,1}^c & 1 - \hat{f}_{0,0}^c & -\hat{f}_{1,-1}^c \\ \hat{g}_{1,1}^c & \hat{g}_{0,2}^c & -\hat{f}_{-1,1}^c & 1 - \hat{f}_{0,0}^c \end{pmatrix} = 0, \quad (30)$$

and

$$\det \begin{pmatrix} 1 - \hat{f}_{0,0} & -\hat{f}_{-1,1} \\ -\hat{f}_{1,-1} & 1 - \hat{f}_{0,0} \end{pmatrix} = 0, \quad \det \begin{pmatrix} 1 - \hat{f}_{0,0}^c & -\hat{f}_{-1,1}^c \\ -\hat{f}_{1,-1}^c & 1 - \hat{f}_{0,0}^c \end{pmatrix} = 0. \quad (31)$$

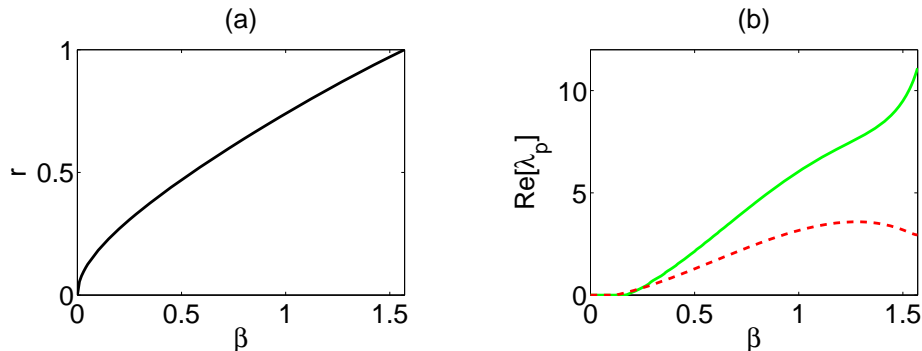


FIG. 5. (Color online) Dependence of (a) the fraction r of coherent oscillators and (b) the real part of the two complex point eigenvalues λ_p on the parameter β .

It turns out that Eq. (30) gives the same result as Eq. (26). This is not so surprising if we compare the elements of the two matrices in Eq. (26) and Eq. (30). These two matrices are almost identical except that some of the matrix elements in Eq. (30) have opposite sign from that of the corresponding terms in Eq. (26). However, this does not affect the final determinant of the matrix. Equation (31) gives two additional branches of eigenvalues, which are complex conjugates of one another. Figure 5(b) shows the dependence of the real part of the two point eigenvalues λ_p that result on the parameter β . As β increases from 0, the red (dashed) eigenvalue λ_p becomes unstable first, at $\beta \approx 0.122$. This onset of instability is consistent with direct numerical simulation.

D. Spiral wave chimeras

For larger values of β , stable configurations of multi-core spiral wave chimera states are found. In this state a core of incoherent oscillators is surrounded by spiral arms consisting of phase-locked oscillators. The arms rotate rigidly with a constant angular velocity. In the following we define the time-averaged oscillation frequency $\bar{\theta}_t(x, y) \equiv \lim_{T \rightarrow \infty} [\theta(x, y, T) - \theta(x, y, 0)]/T$ at each location on the torus. From the self-consistency analysis, we then find that $\bar{\theta}_t(x, y) = -\Omega$ when $\Omega < R(x, y)$ (the coherent region outside the core) and $\bar{\theta}_t(x, y) = -\Omega + \sqrt{\Omega^2 - R(x, y)^2}$ when $\Omega > R(x, y)$ (in the incoherent core). The former frequency thus corresponds to the angular velocity of the spiral arms, i.e., to the rotation rate of the *spatial* pattern; the latter frequency depends on the distance from the core (it vanishes at the core center where $R = 0$) but because the core is incoherent the frequency cannot be identified with spatial rotation. Figure 6 shows the phase distribution in multi-core spiral chimeras obtained with the coupling kernels $G_1^{(1)}$ and $G_2^{(1)}$, specifically with 4 and 16 incoherent cores, distributed evenly in both x and y directions. In addition, Figure 7 shows three examples of spiral wave chimeras with $G_1^{(1)}$ and different values of β . These results indicate that spiral wave chimeras can be present for α near $\pi/2$, in contrast to earlier work suggesting that such states would only be found for α sufficiently close to zero

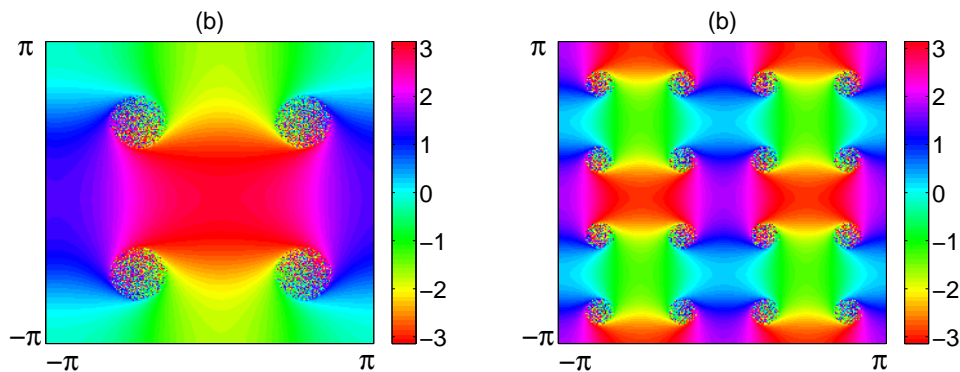


FIG. 6. (Color online) Snapshots of the phase patterns for two numerically stable spiral wave chimera states. (a) The phase distribution $\theta(x, y)$ for $G_x = G_y = G_1^{(1)}$. (b) The phase distribution $\theta(x, y)$ for $G_x = G_y = G_2^{(1)}$. The upper left spirals rotate clockwise in both (a) and (b), with the direction of rotation alternating from core to core in both x and y directions. The phase patterns have the symmetry D_2 and not D_4 . Simulations are done with $\beta = 1$, $N = 256$ and random initial conditions. Colors indicate the phase of the oscillators.

[13].

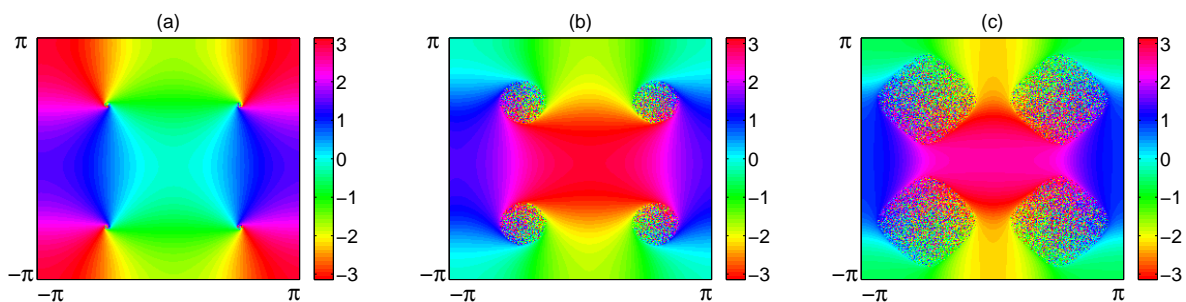


FIG. 7. (Color online) Snapshots of the phase patterns for spiral wave chimeras. (a) $\beta = 1.5$. (b) $\beta = 1$. (c) $\beta = 0.5$. In all three panels, colors indicate the phase of the oscillators. The simulations are done with $G_x = G_y = G_1^{(1)}$, $N = 256$ and random initial conditions.

To understand the origin of the $n = 1$ spiral wave chimeras, we examine their properties using the self-consistency analysis. It turns out (Appendix B) that $R \exp(i\Theta) = b(\sin(x) + i \sin(y))$ and hence that

$$2b^2 = \exp(i\beta) \left\langle \Omega - \sqrt{\Omega^2 - b^2(\sin^2 x + \sin^2 y)} \right\rangle. \quad (32)$$

The right side of Eq. (32) remains unchanged when $\sin^2 x$ and $\sin^2 y$ are replaced by $\sin^2(px)$ and $\sin^2(qy)$ for all $p, q \in \frac{1}{2}\mathbb{N}$. Solving Eq. (32) gives us the values of Ω and b for the $m = 1$ spiral wave chimera, where m is the azimuthal wave number of the spiral. Thus $|\Omega|$ is also the rotation frequency of the spiral in *space*.

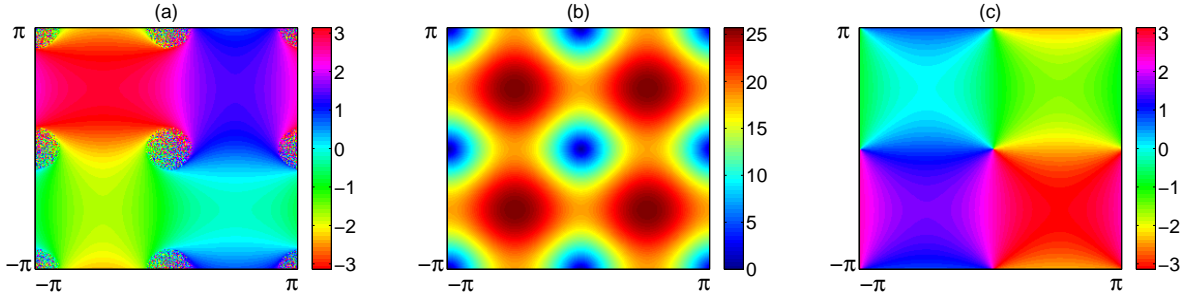


FIG. 8. (Color online) (a) Snapshot of the phase distribution $\theta(x, y)$ for a four-core spiral wave chimera state for $\beta = 1$ (Fig. 7(b)) after translation of one of the incoherent cores to the origin. (b) The corresponding order parameter $R(x, y)$. (c) The corresponding order parameter $\Theta(x, y)$. The simulation is done with $G_x = G_y = G_1^{(1)}$, $N = 256$ and random initial conditions. In panels (a) and (c) colors indicate the phase of the oscillators; in (b) color indicates the amplitude of the local order parameter $R(x, y)$.

When $\beta = \frac{\pi}{2}$, we obtain $\Omega = 0$ and $b = \langle \sqrt{\sin^2 x + \sin^2 y} \rangle / 2 \approx 18.91$. Figure 9(a) shows the dependence of b and Ω on β . As β decreases from $\frac{\pi}{2}$, b decreases, Ω increases and the area of incoherent cores increases. When $\beta \approx 0.38$, $b = \Omega$ and the incoherent cores touch each other (Fig. 10(b)). When β decreases further, the incoherent domains reconnect and the coherent domains separate into four isolated islands (Fig. 10(c)).

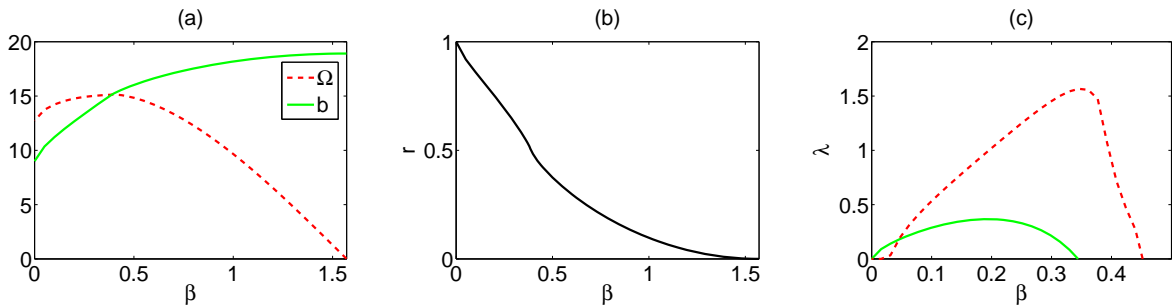


FIG. 9. (Color online) Dependence on the parameter β of (a) b , Ω , (b) the fraction r of incoherent oscillators, and (c) unstable point eigenvalues λ_p , computed from Eq. (33) (green solid line) and Eq. (34) (red dashed line).

The stability of spiral wave chimera states can be analyzed in the same way as for the $2n$ -cluster chimeras and twisted chimeras. Again, when $n = 1$, the point eigenvalue λ_p is determined by Eq. (25). It turns out that the determinant in Eq. (25) factors into three factors:

$$\det \begin{pmatrix} 1 - \hat{f}_0 - \hat{f}_2 & \hat{g}_2 \\ \hat{g}_2^c & 1 - \hat{f}_0^c - \hat{f}_2^c \end{pmatrix} = 0, \quad (33)$$

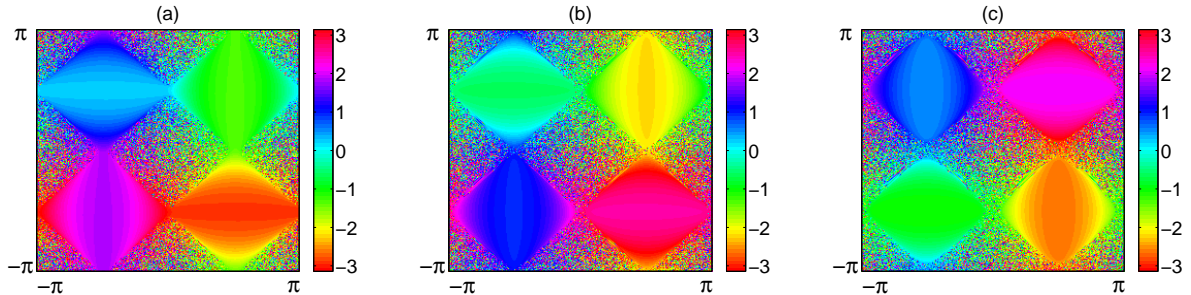


FIG. 10. (Color online) Snapshots of the phase patterns for spiral wave chimeras showing localized regions of coherence embedded in an incoherent background. (a) $\beta = 0.4$. (b) $\beta = 0.38$. (c) $\beta = 0.36$. In all three panels, colors indicate the phase of the oscillators. The simulations were done for gradually decreasing β and $G_x = G_y = G_1^{(1)}$, $N = 256$.

$$\det \begin{pmatrix} 1 - \hat{f}_0 + \hat{f}_2 & -2\hat{g}_1 - \hat{g}_2 \\ -2\hat{g}_1^c - \hat{g}_2^c & 1 - \hat{f}_0^c + \hat{f}_2^c \end{pmatrix} = 0, \quad (34)$$

$$\det \begin{pmatrix} 1 - \hat{f}_0 + \hat{f}_2 & 2\hat{g}_1 - \hat{g}_2 \\ 2\hat{g}_1^c - \hat{g}_2^c & 1 - \hat{f}_0^c + \hat{f}_2^c \end{pmatrix} = 0, \quad (35)$$

of which the first block appears twice.

Solving these three equations determines the number of point eigenvalues and their dependence on β , just as in the case of the $2n$ -cluster chimeras and the twisted chimeras. We plot the unstable eigenvalues in Fig. 9(c). The green solid line is computed from Eq. (33) and corresponds to an eigenvalue of double multiplicity while the red dashed line is computed from Eq. (34); Eq. (35) does not generate unstable eigenvalues. Figure 9(c) indicates an onset of instability already at $\beta \approx 0.46$ as β decreases. However, in numerical simulations we find that the spiral state remains stable down to $\beta = 0.349$, and no signature of an instability onset at $\beta \approx 0.46$ was identified despite long integration times. Figure 11(a) shows that the amplitude of the predicted unstable mode for $0.349 \lesssim \beta \lesssim 0.46$ has a pair of reflection symmetries in the two diagonals, suggesting that the unstable mode enlarges the spirals along one diagonal, while compressing those along the other, thereby breaking the D_4 symmetry of the core locations. In our simulations for $0.4 \leq \beta \leq 0.5$ this collective instability appears to have an amplitude that is so small that it is masked by fluctuations due to the finite number of oscillators used in the simulations (we have used up to 512×512 oscillators). In contrast, the instability predicted from Eq. (33) to be at $\beta \approx 0.344$ (Fig. 9(c), green solid line) is easily detectable and agrees quite well with the numerically determined onset, $\beta \approx 0.349$. Figure 12 shows the corresponding eigenfunctions; since the multiplicity of this eigenvalue is two, there are two linearly independent eigenfunctions, and these enhance the spirals along the x or y axes, in contrast to those along the diagonals.

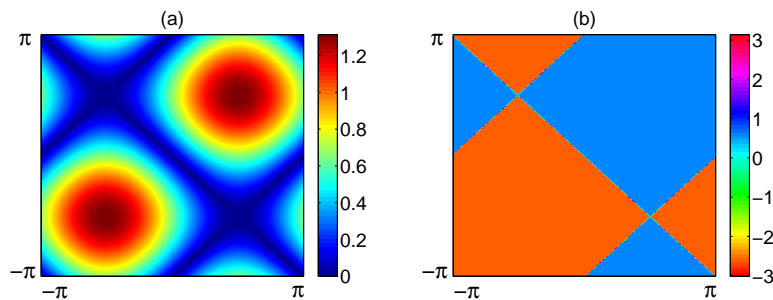


FIG. 11. (Color online) (a) Modulus and (b) phase of the unstable eigenvector $v(x, y)$ of the state shown in Fig. 8(a) when $\beta \approx 0.41$. The corresponding eigenvalue is $\lambda_p \approx 0.717$ as computed from Eq. (34).

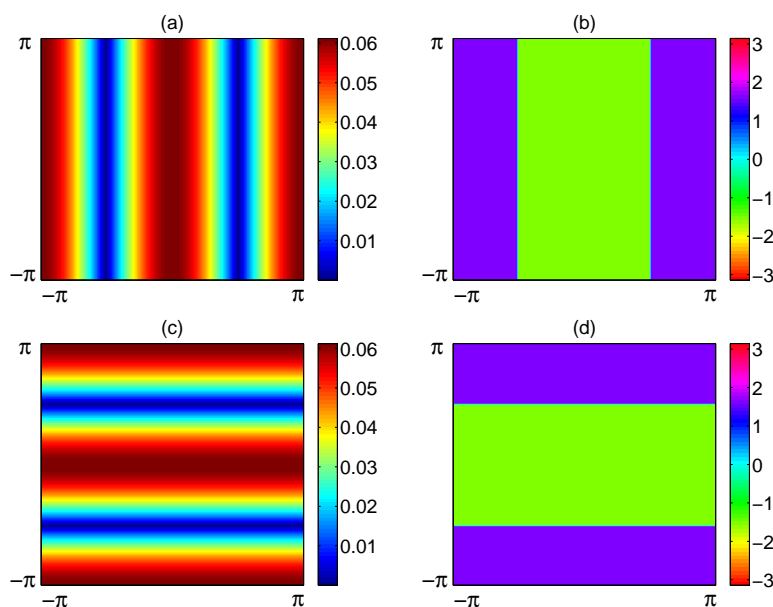


FIG. 12. (Color online) (a,c) Modulus and (b,d) phase of the unstable eigenvectors $v(x, y)$ of the state shown in Fig. 8(a) when $\beta \approx 0.33$. The corresponding eigenvalue is $\lambda_p \approx 0.083$ as computed from Eq. (33).

IV. THE CASE $G_x = G_y = G_n^{(2)}$

In this section, we consider the coupling kernel with $G_x = \cos(nx) + \cos[(n+1)x]$ and $G_y = \cos(ny) + \cos[(n+1)y]$. Much richer dynamics are observed.

A. Inherited solutions

With $G_x = \cos(nx) + \cos[(n+1)x]$ and $G_y = \cos(ny) + \cos[(n+1)y]$ 1D splay states with twist number $|q| = n$ and $|q| = n+1$ are again observed (not shown). All other splay states are linearly unstable.

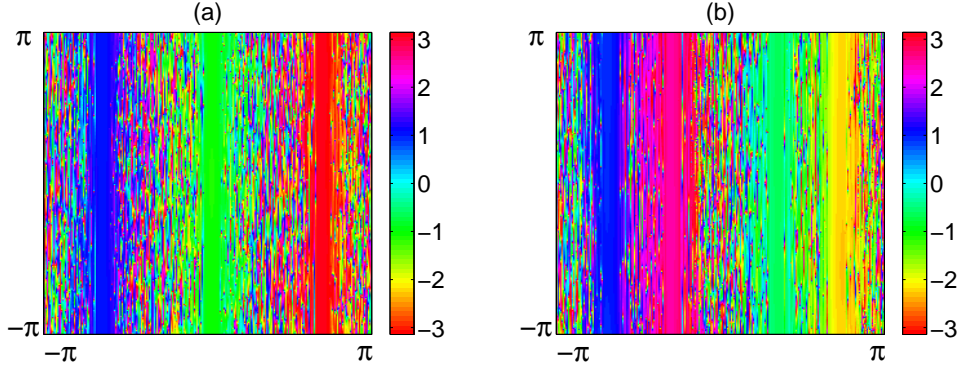


FIG. 13. (Color online) Snapshot of the phase pattern for (a) a 3-cluster chimera state, and (b) a 4-cluster chimera state, both for $G_x = G_y = G_1^{(2)}$, $\beta = 0.05$ and $N = 256$, but starting from different but random initial conditions.

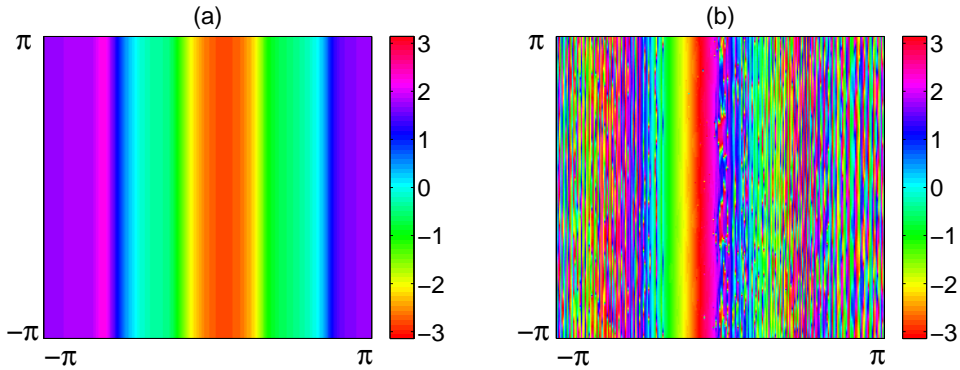


FIG. 14. (Color online) (a) Snapshot of the phase pattern in a right-traveling coherent state. The simulation is done for $G_x = G_y = G_1^{(2)}$, with $\beta = 0.7$ and $N = 256$. (b) Snapshot of the phase pattern for a right-traveling chimera state. The simulation is done for $G_x = G_y = G_3^{(2)}$, with $\beta = 0.03$ and $N = 256$.

In addition to the splay states, many of the other states observed in the 1D system [5] have counterparts that are stable in two dimensions. Examples of 1D-like 3-cluster and 4-cluster chimeras are shown in Fig. 13, while a traveling coherent state and a traveling chimera state are shown in Fig. 14.

B. Twisted chimera states

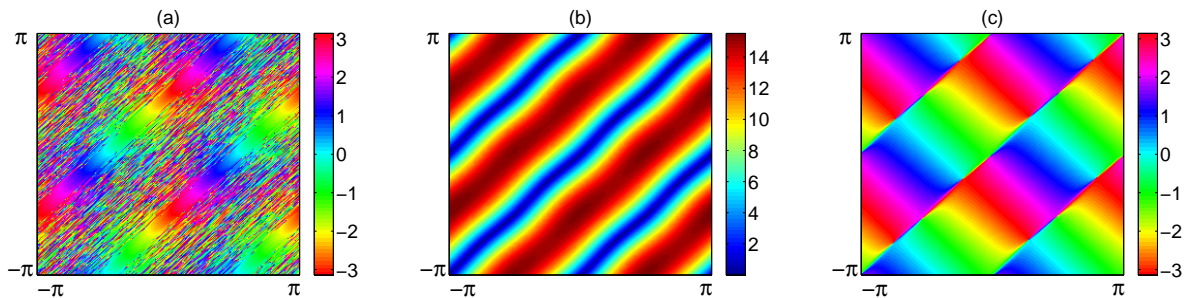


FIG. 15. (Color online) (a) Snapshot of the phase distribution in a 2:2 twisted chimera state. (b,c) The local order parameters R and Θ computed from (a). The simulation is done for $G_x = G_y = G_1^{(2)}$, with $\beta = 0.05$, $N = 256$ and random initial condition.

When $G_x = \cos(nx) + \cos[(n+1)x]$ and $G_y = \cos(ny) + \cos[(n+1)y]$, three types of twisted chimera states are observed, $n : n$ twisted chimeras, $n+1 : n+1$ twisted chimeras and $n : n+1$ twisted chimeras. In the following, we use the case $n = 1$ to illustrate these states and the associated self-consistency analysis. The 1:1 twisted chimera looks identical to Fig. 3, while Figs. 15 and 16 show the phase distribution and the local order parameter for a 2:2 and a 1:2 twisted chimera, respectively.

The self-consistency analysis shows that for 2:2 twisted chimera, the local order parameter takes the form $\tilde{Z}(x, y) = \frac{R_0}{2}(\exp(2ix) - \exp(2iy))$ with

$$R_0^2 = \exp(i\beta) \left\langle \Omega - \sqrt{\Omega^2 - R_0^2 \sin^2(x-y)} \right\rangle, \quad (36)$$

while for the 1:2 twisted chimera the local order parameter has the form $\tilde{Z}(x, y) = \frac{R_0}{2}(\exp(ix) - \exp(2iy))$ with

$$R_0^2 = \exp(i\beta) \left\langle \Omega - \sqrt{\Omega^2 - R_0^2 \sin^2(x/2 - y)} \right\rangle. \quad (37)$$

The derivation of these relations can be found in Appendix C. Both are equivalent to Eq. (19) after change of variables.

The 1:1 chimera states correspond to the local order parameter $\tilde{Z} = \frac{R_0}{2}(\exp(ix) - \exp(iy))$ and the self-consistency equation is identical to Eq. (29). The derivation of Eq. (29) (for a 1:1 twisted chimera), Eq. (36) (for a 2:2 twisted chimera) and Eq. (37) (for a 1:2 twisted chimera) shows that even if multiple Fourier components are included in the coupling kernel ($G_x = G_y = G_1^{(2)}$), some of these do not contribute to the final result owing to the symmetries of the solution. However, the stability properties of the corresponding states may be affected. For the three types of twisted chimera states discussed above, the stability is determined by point eigenvalues satisfying $\det \mathbf{B}(\lambda_p) = 0$, where $\mathbf{B}(\lambda_p)$ is defined in Eq. (24). In the present case, the corresponding matrices \mathbf{B} are 16×16 matrices. It turns out that these

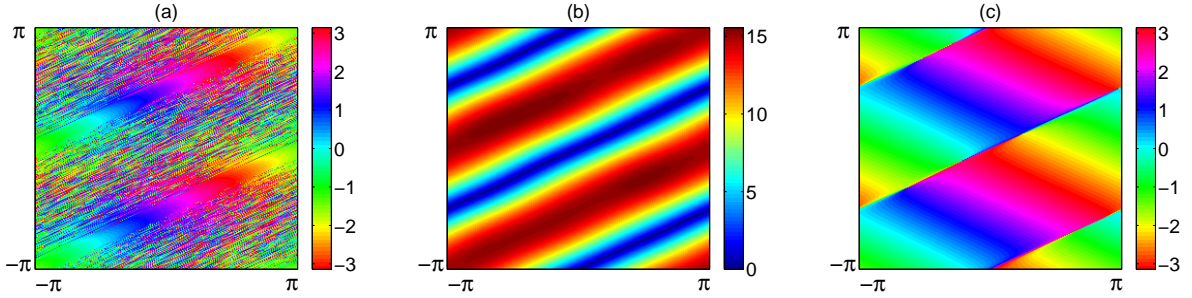


FIG. 16. (Color online) (a) Snapshot of the phase distribution in a 1:2 chimera state. (b,c) The local order parameters R and Θ computed from (a). The simulation is done for $G_x = G_y = G_1^{(2)}$, with $\beta = 0.05$, $N = 256$ and random initial condition.

share the same point eigenvalues as the 1:1 chimera state for $G_x = G_y = G_1^{(1)}$, which are determined by Eqs. (30) and (31). Additional point eigenvalues may also be present, but these do not affect stability and hence the theory predicts that all three types of twisted chimera lose stability at $\beta \approx 0.122$. This value agrees reasonably well with the instability threshold $\beta = 0.13 \pm 0.01$ obtained from direct numerical simulations.

C. Spiral wave chimeras

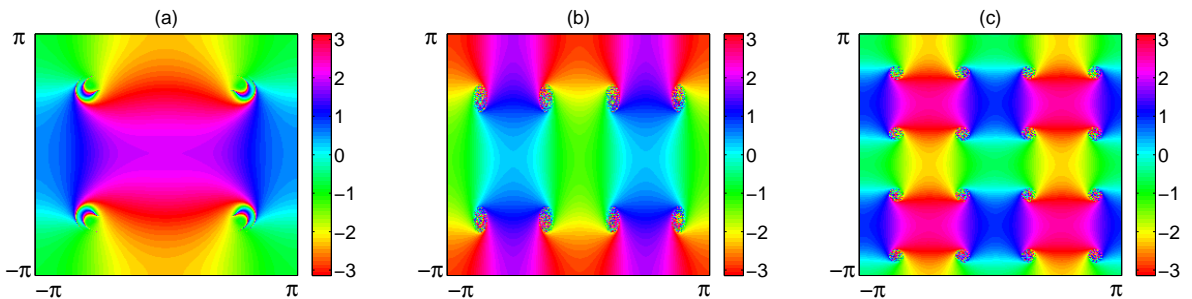


FIG. 17. (Color online) Snapshots of the phase pattern in three numerically stable spiral wave chimeras. (a) 4 intermittently incoherent cores. (b) 8 incoherent cores. (c) 16 incoherent cores. The simulation is done for $G_x = G_y = G_1^{(2)}$, with $\beta = 1.2$, $N = 256$ and random initial conditions.

Multi-core spiral wave states are also observed for $G_x = \cos(nx) + \cos[(n+1)x]$, $G_y = \cos(ny) + \cos[(n+1)y]$ and some examples are given in Fig. 17. The states shown in Figs. 17(b,c) are similar to the spiral wave chimera states for $G_x = \cos(nx)$, $G_y = \cos(ny)$; in particular the spiral arms rotate with constant angular velocity given by the time-averaged oscillator frequency $\bar{\theta}_t(x, y)$ introduced in section III D. The complex order parameter for these states can also be reduced to simpler form by appropriate symmetry arguments and it turns out that for the solutions in Figs. 17(b,c) it takes the form $\tilde{Z}(x, y) = b_2(\sin(kx) +$

$i \sin(l y))$ with $k = 2$ and $l = 1, 2$. The final self-consistency equation, viz.,

$$2b_2^2 = \exp(i\beta) \left\langle \Omega - \sqrt{\Omega^2 - b_2^2(\sin^2(kx) + \sin^2(l y))} \right\rangle, \quad (38)$$

is equivalent to Eq. (32).

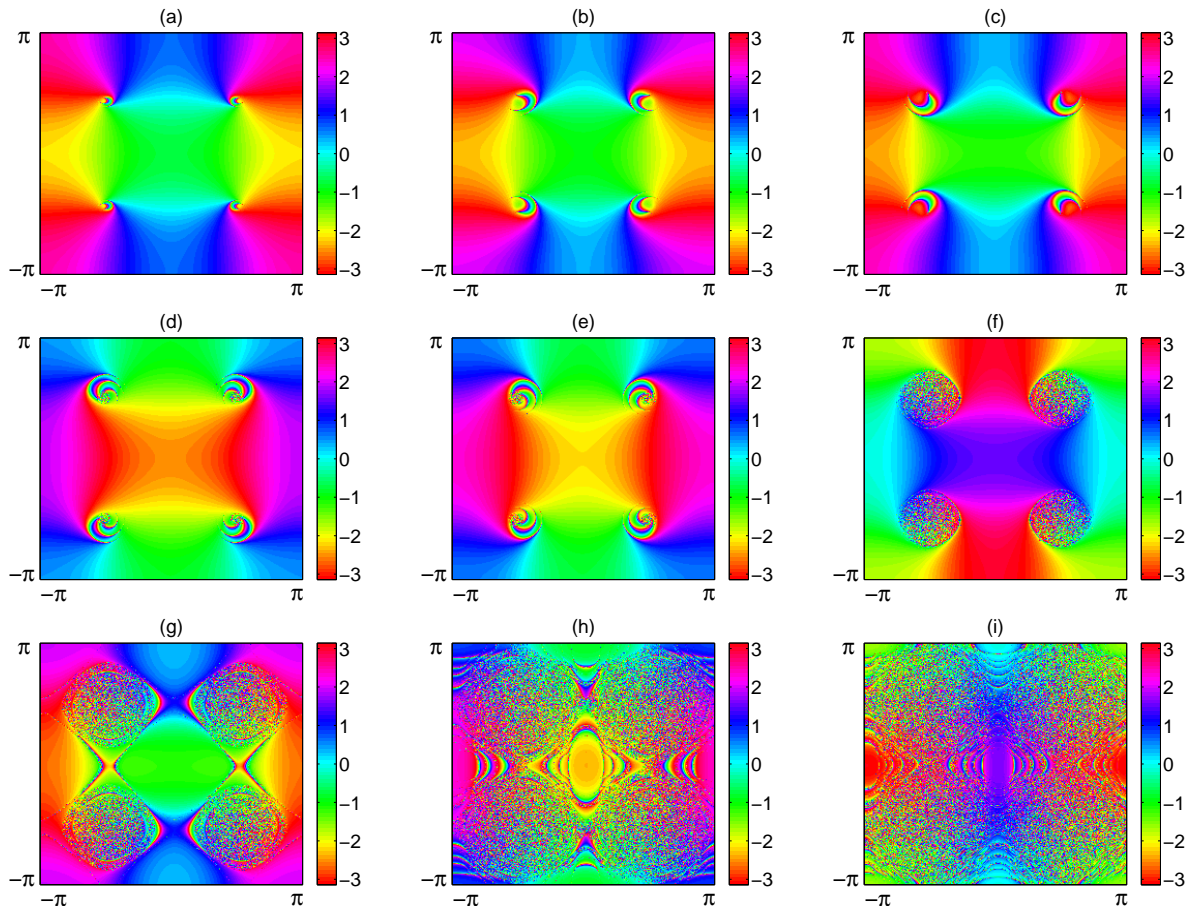


FIG. 18. (Color online) Snapshots of chimera states for $G_x = G_y = G_1^{(2)}$, $N = 256$, obtained by gradually decreasing β . (a) $\beta = 1.4$. (b) $\beta = 1.2$. (c) $\beta = 1.118$. (d) $\beta = 1.117$. (e) $\beta = 1.1$. (f) $\beta = 0.8$. (g) $\beta = 0.4$. (h) $\beta = 0.06$. (i) $\beta = 0.025$.

The state shown in Fig. 17(a) is particularly interesting. Unlike the other two spiral wave states shown in Figs. 17(b,c) the cores of the state in Fig. 17(a) are incoherent only intermittently; these partially or intermittently incoherent regions are not stationary but rotate in the same sense as the coherent state to the outside but rather more slowly. We illustrate this behavior using an example for $\beta = 1.4$. For this value of β , a snapshot of the phase pattern at a particular instant is shown in panel (a) of Fig. 18. We should emphasize that no persistently incoherent cores have as yet developed. Analysis of snapshots of the phase distribution along a slice through one of the cores reveals the presence of a group of oscillators in the core region that alternately detrain and then entrain as the incoherent oscillators

precess around the core (Fig. 19). The figure suggests that the detrain/entraining process is approximately periodic (i.e., that the precession takes place at a constant angular speed), much as is the case for a similar process observed in one-dimensional oscillator arrays in [5]. The resulting repeated detrain and entraining at a fixed location implies that the phase distribution in the core is not time-independent and hence that a self-consistency analysis based on the assumption that the order parameters are time-independent must necessarily fail as soon as the number of oscillators undergoing this process becomes substantial as found in 1D in Ref. [5].

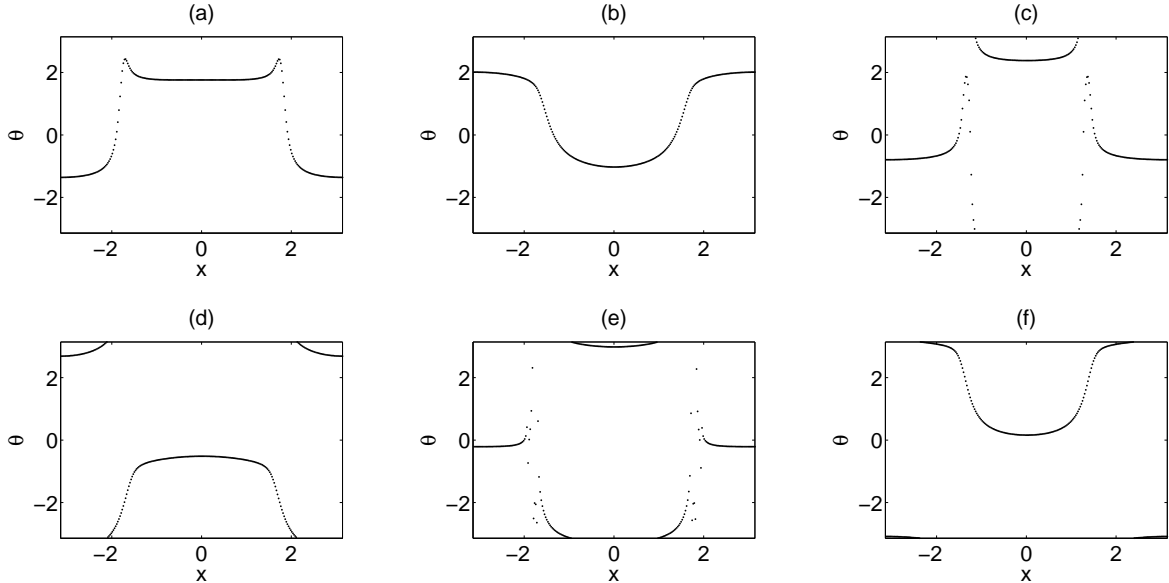


FIG. 19. Snapshots of the phase pattern $\theta(x, y_0, t)$ for $G_x = G_y = G_1^{(2)}$, with $N = 256$ and $\beta = 1.4$. (a) $t = 0$. (b) $t = 5$. (c) $t = 10$. (d) $t = 15$. (e) $t = 20$. (f) $t = 25$. Here, panel (a) is a slice through the upper two cores of Fig. 18(a) and so are the remaining panels. Note the significant detrain of some oscillators in panels (c) and (e).

Starting from a 4-core spiral wave at $\beta = 1.57$ we decreased β in steps of $\Delta\beta = 0.001$. For each β , the simulation was run for $T = 250$, corresponding to between 120 and 600 rotation periods of the spiral, depending on β ($0 < \beta < 1.4$, see Fig. 9(a)). Figure 18 shows snapshots of the states observed for different values of β . When $\beta \gtrsim 1.118$, the partially incoherent cores exhibit crescent phase structure with $m = 1$ azimuthal wave number. At $\beta \approx 1.118$ the azimuthal mode number m of this state jumps from $m = 1$ to $m = 2$, and once $\beta \lesssim 1.117$ fully incoherent inner cores are present, surrounded in the outer core with an intermittent partially coherent state corresponding to an $m = 3$ spiral pattern (Fig. 18(d)). As β decreases further, the fully incoherent inner cores grow in extent and swallow the outer core arms one by one (Fig. 18(f)). In contrast, the azimuthal wave number in the coherent domain outside the core remains $m = 1$ throughout the range of β examined with the $m = 1$ arm rotating clockwise in the upper right and bottom left and counter-clockwise in the upper left and bottom right of each panel. The arms of the partially coherent or

incoherent cores rotate in the same sense, but with a substantially slower angular velocity than in the coherent domain. All these states are numerically stable.

The crescent structures observed here with the coupling kernels $G_1^{(2)}$ are associated with the partially incoherent spiral cores, and are reminiscent of similar structures observed in unpublished work by Omel'chenko and Wolfrum, and also by Strogatz and in 3D by Maistrenko *et al.* [12], in all cases with different coupling kernel G . In the work of the former authors these structures appear to be associated with the onset of a core instability, typically an unstable meander. This fact has led us to investigate carefully the presence of possible meandering instabilities of the spiral cores for our parameter values, but without success – in the present work these structures are numerically stable (some of our integrations were continued for $T = 10000$ without finding any instability). Moreover Ref. [12] identifies similar structures in 3D and these are also apparently stable. Thus the crescent structures appear to be an equilibrium phenomenon, at least in the present work, and so merit further study.

When β is decreased yet further a new set of oscillators, surrounding the incoherent core, start detrainning for a certain time interval before entraining again. As a result the snapshot shown, for example, in Fig. 18(g) fluctuates in time. The intermittent incoherence is located along a vein-like structure surrounding the cores and its location oscillates around the incoherent core as time progresses. The size of the incoherent core appears to be independent of N although fluctuations arising from the use of a finite number of oscillators in the simulations are inevitably present. When β reaches $\beta \approx 0.06$, the incoherent regions begin to merge (Fig. 18(h)) and, with decreasing β , incoherence invades a larger and larger portion of the two-torus (Fig. 18(i)). The partially coherent state finally loses stability at $\beta \approx 0.024$ and evolves into a twisted chimera state. The process described above exhibits some hysteresis – to confirm this we performed a simulation with β increasing from small values in steps of size $\delta\beta = 0.001$ and for each β the simulation was run for total time $T = 250$. The transitions reflected in Fig. 18 do not occur at identical β values. Figure 20 shows snapshots of the states for different values of β when β is gradually increased. The fully incoherent cores disappear at $\beta \approx 1.25$, a value that differs from the value $\beta \approx 1.117$ for the corresponding transition when β is gradually decreased.

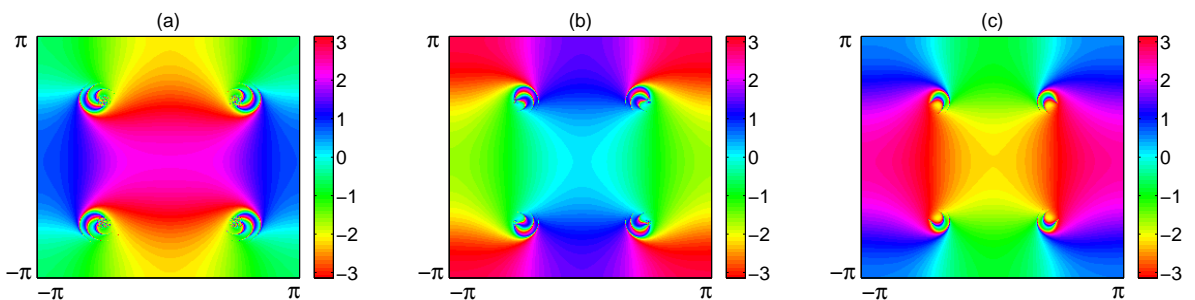


FIG. 20. (Color online) Snapshots of chimera states for $G_x = G_y = G_1^{(2)}$, $N = 256$ and (a) $\beta = 1.12$. (b) $\beta = 1.2$. (c) $\beta = 1.25$, obtained on increasing β in steps of $\delta\beta = 0.001$ and integrating for $T = 250$ before the next increase.

Figure 21 shows plots of the time-averaged frequency $\bar{\theta}_t(x, y)$ for different values of β and provides more information about the regions of detraining/entraining oscillators. Compared with the completely phase-random region, where $\bar{\theta}_t$ gradually increases (in absolute value) from the center of an incoherent core towards the coherent region, $\bar{\theta}_t$ in the detraining/entraining regions varies in a step-wise fashion, and not necessarily monotonically (Fig. 21(a,b)). The vein-like structure surrounding the cores for certain values of β also becomes clear (eg., Fig. 21(g)).

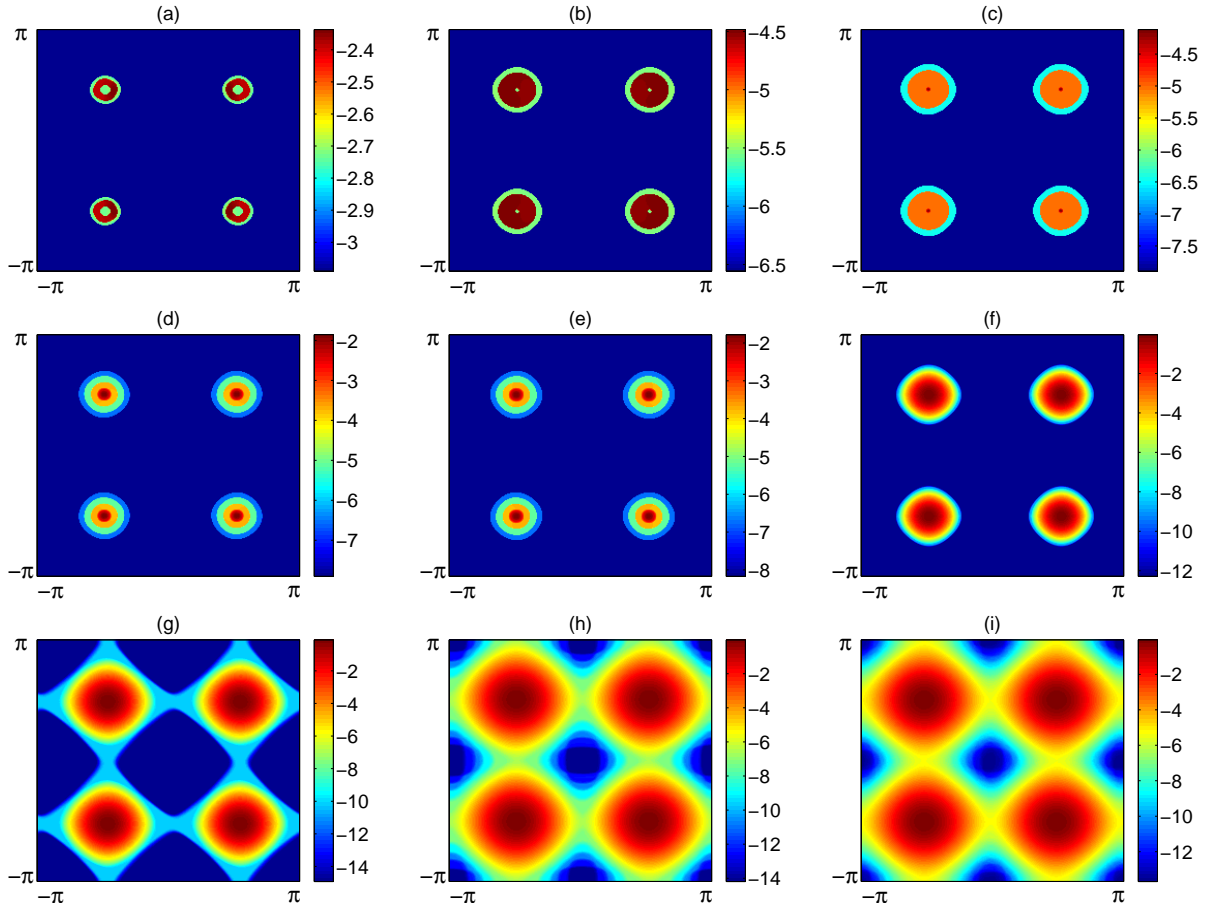


FIG. 21. (Color online) Snapshots of the oscillator frequency $\bar{\theta}_t(x, y)$ averaged over the time interval $0 \leq t \leq 250$ for $G_x = G_y = G_1^{(2)}$, and $N = 256$. (a) $\beta = 1.4$. (b) $\beta = 1.2$. (c) $\beta = 1.118$. (d) $\beta = 1.117$. (e) $\beta = 1.1$. (f) $\beta = 0.8$. (g) $\beta = 0.4$. (h) $\beta = 0.06$. (i) $\beta = 0.025$.

A figure analogous to Fig. 21(a,b) but with $N = 512$ (not shown) confirms that the nonmonotonic behavior is not a finite size effect. In addition, we plot the behavior of $\bar{\theta}_t$ as a function of the distance d to the center of the core for different values of β (Fig. 22). As the cores are not exactly circular, we pick two directions as representative. In Fig. 22(a), we pick a horizontal cut through a core, and denote the distance to the center of the core as d_h . In Fig. 22(b), we pick instead a diagonal cut through a core, and denote the distance to the center as d_d . The behavior of $\bar{\theta}_t$ in these two cases is quite similar: $\bar{\theta}_t$ varies in general in a step-wise fashion, but not necessarily monotonically. When $\beta = 0.8$, the core is completely

incoherent and the variation of $\bar{\theta}_t$ is similar to the case described in III D. Apart from nonmonotonic behavior, we also noticed that in a certain range of β the oscillator frequency at the center of a core remains nonzero (eg., Fig. 21(a)–(e)). To see in detail how the phase oscillates in the core area, we investigate the dynamical behavior for particular oscillators when $\beta = 1.1$. It turns out that even in the center of a fully incoherent core the phase oscillates with a nonzero frequency, in contrast to the spiral wave chimeras described in III D. We plot θ as a function of t for different distances d_h from the core (horizontal cut) in Fig. 23. Figure 23(a) confirms that $\bar{\theta}_t \neq 0$ in the center of the core, and reveals in addition that the frequency fluctuates relative to a nonzero mean with a characteristic fluctuation time scale. The origin of this time scale is not clear. Figures 23(b,c) show the behavior of oscillators in the partially incoherent region farther from the core center. The figures reveal that the oscillators at this location undergo episodic frequency fluctuations; between these episodes the oscillation frequency remains constant. We identify these episodes (which appear to recur periodically) with the detrainning/entraining events mentioned above and conclude that at this location the spatial phase pattern undergoes episodic rigid rotation. The duration of the detrainning/entraining events decreases as d_h increases and they are absent in the fully coherent region farther out (Fig. 23(d)). At the same time the mean oscillation frequency $\bar{\theta}_t(x, y)$ gradually increases to its value Ω characterizing the fully coherent region.

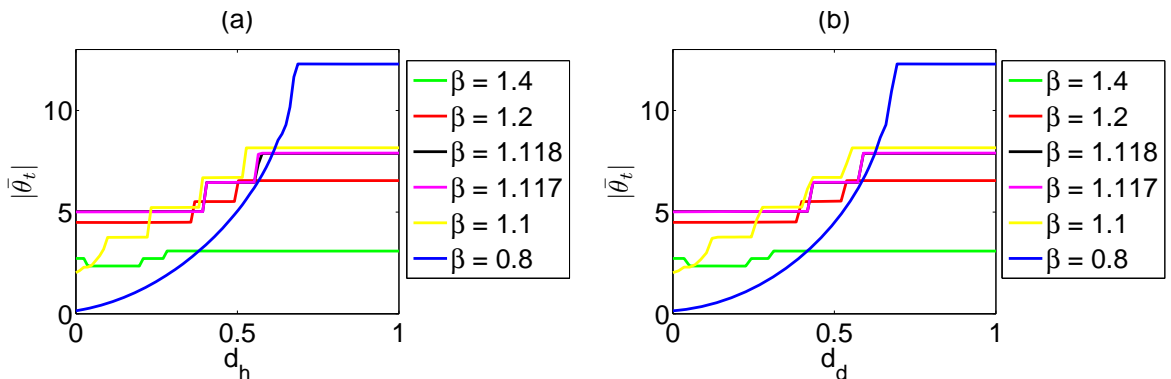


FIG. 22. (Color online) The mean oscillation frequency $\bar{\theta}_t$ as a function of (a) the horizontal distance d_h , (b) the diagonal distance d_d from the center of a core for different values of β , showing a stepwise but monotonic dependence for $0.8 \lesssim \beta \lesssim 1.2$ and a stepwise nonmonotonic dependence for $\beta = 1.4$. The dependence for $\beta = 0.8$ is continuous all the way to the core radius. The curves for $\beta = 1.117$ and $\beta = 1.118$ almost overlap.

To gain a partial understanding of the above results we note that in certain intervals of β ($0.8 \gtrsim \beta \gtrsim 0.45$), the multi-core spiral wave states in Fig. 18 are similar to the states found with $G_x = \cos(x)$, $G_y = \cos(y)$ for which the self-consistency analysis proved successful. Since Eq. (10) is invariant under translations in x and y directions, we choose the origin of coordinates such that the computed $R(x, y)$ and $\Theta(x, y)$ are (at least, approximately) invariant under the pair of reflections $(x, y) \rightarrow (-x, y)$ and $(x, y) \rightarrow (x, -y)$. These symmetries

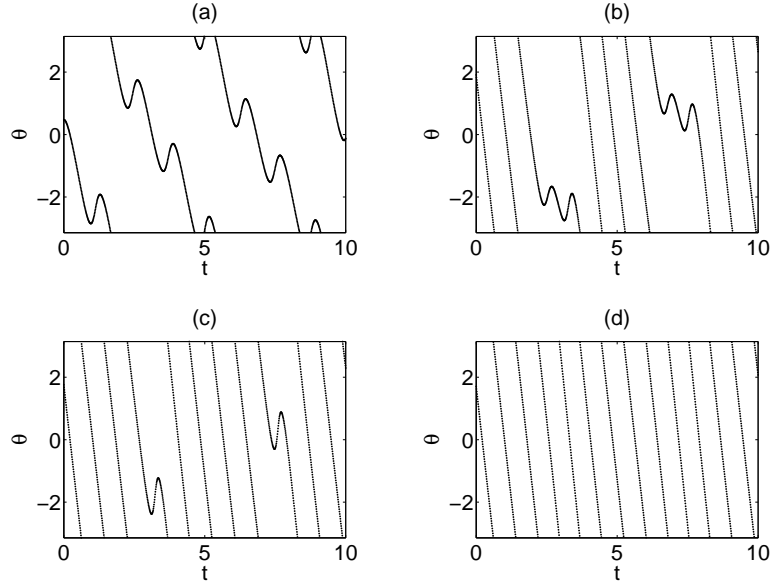


FIG. 23. The phase $\theta(x = d_h, y = 0, t)$ as a function of t for $\beta = 1.1$ and different values of d_h . (a) $d_h = 0$. (b) $d_h = \pi/8$. (c) $d_h = 3\pi/16$. (d) $d_h = \pi/4$.

allow us to write

$$R \exp(i\Theta) = a_1 \cos(x) + c_1 \cos(y) + a_2 \cos(2x) + c_2 \cos(2y). \quad (39)$$

When β is around 0.8, as in the 4-core spiral wave chimera state for $G_x = \cos(x)$, $G_y = \cos(y)$, we can assume in addition that the local order parameter R is invariant under the reflection $(x, y) \rightarrow (y, x)$, at least approximately. Alternatively, we can solve for a_1 , c_1 , a_2 and c_2 directly without making use of this additional symmetry. The result is $\Omega \approx 12.284$, $a_1 \approx 17.533$, $c_1 \approx 17.533i$, $a_2 = 0$, and $c_2 = 0$. For comparison, the order parameter computed directly from the simulation data has $a_1 \approx 18.1$. However, in view of the narrow spiral structures along the core edge (Fig. 18(f)) one cannot expect accurate agreement between the simulation and the theory at this value of β . In fact the theory appears to work better for smaller β . For example, when $\beta = 0.7$, $a_1 \approx 17.11$ from the self-consistency equation, compared with the value $a_1 \approx 17.15$ from simulation. Nonetheless, we emphasize that the self-consistency requirement must be regarded as an approximation that is valid only in a certain range of β . In other regimes the self-consistency equation fails to account for the more exotic chimera states observed there. This is for the following reasons:

- If the self-consistency analysis is correct, the oscillators in the incoherent core should be locally uncorrelated. However, Figs. 18(a)–(e) show that this is not the case.
- The self-consistency analysis requires that the local order parameter R vanishes at the phase singularity point at the core center (x_0, y_0) . It therefore predicts that $\partial\theta(x_0, y_0, t)/\partial t = \Omega$ in the rotating frame, or equivalently that $\bar{\theta}_t(x_0, y_0) = 0$ in the original frame. However, numerical calculations show that this is also not the case (e.g., Fig. 21(a)–(e)).

These reasons are similar to those that were found to apply to phase-coupled oscillators in one-dimensional arrays in the presence of intermittent detrainning. In one dimension it was possible to confirm that these oscillations were intrinsic to the system and hence not an artifact of a finite oscillator number [5]. It is considerably harder to confirm that this continues to be the case in two dimensions, although we believe that this is in fact the case – computations with an 512×512 oscillator array yield results very similar to those obtained for a 256×256 array.

For these reasons we have not attempted a stability calculation of the above states using the postulated order parameter expressions along the lines of Sec. III.

V. DISCUSSION AND CONCLUSIONS

In this paper we have investigated a two-dimensional system of identical phase-coupled oscillators with nonlocal coupling of indefinite sign. We focused on the case where the coupling kernel $G(x, y)$ is D_4 symmetric and can be written in the form $G(x, y) = G_x(x) + G_y(y)$. As in [5], G_x and G_y are chosen from two families of coupling kernels, $G_n^{(1)}(x) \equiv \cos(nx)$ and $G_n^{(2)}(x) \equiv \cos(nx) + \cos[(n+1)x]$. We found that the stationary solutions in the corresponding one-dimensional system (15) have counterparts in two dimensions, although their stability properties may differ owing to the possible presence of unstable longitudinal modes. For example, $2n$ -cluster chimera states were shown to be unstable in 2D for all values of β , while they are stable for certain range of β in 1D systems. In addition to these expected states we also found a class of twisted chimera states in which the phase varies uniformly along a closed coherent stripe, and a class of spiral wave chimera states in which cores of incoherent oscillators are surrounded by coherent rigidly rotating spiral arms. With the coupling kernels we have used, these chimeras are quite common and robust in the sense that they can be obtained starting from random initial conditions.

We have obtained a fairly complete description of the above-mentioned stationary phase patterns using a self-consistency analysis based on Eq. (10). Symmetry arguments allowed us to reduce Eq. (10) to several algebraic equations. The local order parameters obtained using this approach agree well with those generated from direct simulations. In addition the loss of stability of these states with respect to β was found to be predicted accurately from the linearization of Eq. (4) describing the evolution of the local mean field. The results obtained are consistent with direct simulations when β is changed gradually. A key input into the analysis was the D_4 symmetry of the coupling kernel $G_n^{(1)}$. It would be of interest therefore to perform a similar study of other D_4 symmetric coupling kernels in order to determine whether these support similar states. We note that none of our states exhibit the D_4 symmetry of the coupling kernel, and surmise that all such states are unstable.

The more exotic spiral wave chimera states were found to be present for the coupling kernel $G_x = G_y = G_n^{(2)}$ and their properties were investigated both decreasing and increasing β . Many of the remarkable states identified with this coupling exhibit intermittent detrainning and entraining on the part of a subset of the oscillators similar to that found in one-dimensional oscillator arrays [5]. The presence of this intermittency renders the self-consistency analysis unusable, and a full understanding of these states remains a challenge.

However, despite the absence of instantaneous D_4 symmetry, time-averaged quantities such as the time-averaged oscillation frequency $\bar{\theta}_t(x, y)$ were found to be accurately D_4 symmetric, suggesting that the results on “symmetry on average” obtained by Golubitsky and colleagues [19, 20] for chaotic maps with symmetry could be extended to the nonlocal systems studied here.

Because of the D_4 symmetry of the coupling kernels $G_n^{(1)}$ and $G_n^{(2)}$ (and translation invariance) the spiral states we have found consisted of four or more individual spirals arranged in a periodic lattice. Thus we have not been able to study the properties of a single spiral state in a plane. Such a state is expected to exhibit the symmetry $\tilde{Z}(r, \theta) \rightarrow \tilde{Z}(r, \theta + \phi)$ under rotations $\theta \rightarrow \theta + \phi$. When \tilde{Z} admits the separable form $\tilde{Z} = R(r) \exp(i\Theta(r) + im\theta)$ this requirement translates into $\tilde{Z} \rightarrow \tilde{Z} \exp(im\phi)$. However, this is not the generic case as can easily be seen by taking, for example, $\tilde{Z} = a(r) \exp(i\theta) + b(r) \exp(2i\theta)$. In this case the handedness of the spiral will be reflected in both $R(x, y)$ and in Θ . In our four-spiral states we have not detected any signature of this handedness, neither locally near the spiral cores, not globally. The resulting reflection symmetries of the order parameters R and Θ facilitated greatly the modeling of these quantities, and the subsequent solution of the self-consistency equation, and in some cases the determination of the stability properties of the resulting state as well. We conclude that in these cases the azimuthal dependence of the spiral state is close to sinusoidal. The reasons for this remain unclear.

This paper provides additional insight into chimera states in systems with dimension higher than one. It shows that spiral wave chimeras are natural objects in two dimensions and that these can be stable in a large range of the parameter β (or α), in contrast to [13]. In future work we will study the existence and properties of states of this type in more realistic systems, including coupled arrays of Landau-Stuart oscillators.

ACKNOWLEDGMENT

We are grateful to C. Laing, O. Omel’chenko, S. Strogatz and M. Wolfrum for helpful discussions. This work was supported in part by a National Science Foundation Collaborative Research Grant CMMI-1233692.

Appendix A: Twisted chimera states, $G_x = G_y = G_n^{(1)}$

Here we perform a self-consistency analysis of the twisted chimera states with $G_x = G_y = G_n^{(1)}$ for $n = 1$. First, we notice that Eq. (10) can be written as

$$R(x, y) \exp(i\Theta(x, y)) = a \cos(x) + b \sin(x) + c \cos(y) + d \sin(y), \quad (\text{A1})$$

where a , b , c , and d are complex numbers given by

$$a = \langle \cos(x') \exp(i\beta) \exp(i\Theta(x', y')) h(x', y') \rangle, \quad (\text{A2})$$

$$b = \langle \sin(x') \exp(i\beta) \exp(i\Theta(x', y')) h(x', y') \rangle, \quad (\text{A3})$$

$$c = \langle \cos(y') \exp(i\beta) \exp(i\Theta(x', y')) h(x', y') \rangle, \quad (\text{A4})$$

$$d = \langle \sin(y') \exp(i\beta) \exp(i\Theta(x', y')) h(x', y') \rangle. \quad (\text{A5})$$

Since Eq. (10) is invariant under translation in x and y , we can choose the origin such that $R(x, y)$ is invariant under the transformation $(x, y) \rightarrow (y, x)$, and $\Theta(x, y)$ has a π phase jump across the line $y = x$. This property implies

$$R(y, x) \exp(i\Theta(y, x)) = R(x, y) \exp(i\Theta(x, y) + i\pi), \quad (\text{A6})$$

which is equivalent to

$$a \cos(y) + b \sin(y) + c \cos(x) + d \sin(x) = -(a \cos(x) + b \sin(x) + c \cos(y) + d \sin(y)). \quad (\text{A7})$$

Matching the coefficients of the Fourier components gives $a = -c$ and $b = -d$.

In addition, we find from Fig. 4(b) that $\Theta(x, y)$ decreases linearly along the $(1, 1)$ direction. This behavior is similar to the splay states with a twist number q . In Fig. 4(b), $q = -1$. From Fig. 4(a), we see that R is constant along the $(1, 1)$ direction. Using this property, we obtain

$$R(x + \delta, y + \delta) \exp(i\Theta(x + \delta, y + \delta)) = R(x, y) \exp(i\Theta(x, y) + i\delta), \quad (\text{A8})$$

where δ represents an arbitrary displacement in the $(1, 1)$ direction. From the limit $\delta \rightarrow 0$ we obtain

$$-a \sin(x) + b \cos(x) - c \sin(y) + d \cos(y) = i(a \cos(x) + b \sin(x) + c \cos(y) + d \sin(y)), \quad (\text{A9})$$

implying that $b = ia$ and $d = ic$.

The fact that Eq. (10) is also invariant under translations in Θ allows us finally to choose a to be real and positive. Writing $a = R_0/2$ and substituting the expression $R \exp(i\Theta) = a(\exp(ix) - \exp(iy))$ into Eqs. (A2)–(A5) leads to a single relation

$$R_0^2 = \exp(i\beta) \left\langle \Omega - \sqrt{\Omega^2 - R_0^2 \sin^2 \left(\frac{x-y}{2} \right)} \right\rangle. \quad (\text{A10})$$

Appendix B: Spiral wave chimera states, $G_x = G_y = G_n^{(1)}$

Spiral wave chimera states are also solutions of the self-consistency equations (A2)–(A5). To simplify the analysis, we translate one of the cores to the origin $(x, y) = (0, 0)$ (Fig. 8(a)). Figure 8(c) shows that $\Theta(x, y)$ is constant, $\Theta(x, y) = \Theta_0$, say, along the line segment between the point $(0, 0)$ and the point $(\pi, 0)$. Invariance of Eq. (10) under translation in Θ allows us to set $\Theta_0 = 0$. With this choice, the local order parameters (R, Θ) have the following symmetry:

$$(x, y) \rightarrow (y, x) \implies (R, \Theta) \rightarrow (R, \frac{\pi}{2} - \Theta). \quad (\text{B1})$$

This symmetry property implies that

$$a \cos(y) + b \sin(y) + c \cos(x) + d \sin(x) = i(a^* \cos(x) + b^* \sin(x) + c^* \cos(y) + d^* \sin(y)). \quad (\text{B2})$$

Matching coefficients leads to $a = ic^*$ and $d = ib^*$. In addition, Figs. 8(b,c) suggest the spiral wave chimera has a symmetry under rotation, viz.,

$$(x, y) \rightarrow (-y, x) \implies (R, \Theta) \rightarrow (R, \Theta + \frac{\pi}{2}), \quad (\text{B3})$$

corresponding to

$$a \cos(-y) + b \sin(-y) + c \cos(x) + d \sin(x) = i(a \cos(x) + b \sin(x) + c \cos(y) + d \sin(y)). \quad (\text{B4})$$

Matching coefficients leads to $a = ic$ and $d = ib$. Finally, reflection with respect to the x axis,

$$(x, y) \rightarrow (x, -y) \implies (R, \Theta) \rightarrow (R, -\Theta), \quad (\text{B5})$$

requires that

$$a \cos(x) + b \sin(x) + c \cos(-y) + d \sin(-y) = a^* \cos(x) + b^* \sin(x) + c^* \cos(y) + d^* \sin(y) \quad (\text{B6})$$

and hence implies $a = a^*$, $b = b^*$, $c = c^*$ and $d = -d^*$. Combining these relations we obtain

$$R \exp(i\Theta) = b(\sin(x) + i \sin(y)). \quad (\text{B7})$$

Substituting this expression into Eqs. (A2)–(A5) we find that the expressions in Eqs. (A2) and (A4) vanish, while Eqs. (A3) and (A5) give

$$2b^2 = \exp(i\beta) \left\langle \Omega - \sqrt{\Omega^2 - b^2(\sin^2 x + \sin^2 y)} \right\rangle. \quad (\text{B8})$$

Appendix C: Twisted chimera states, $G_x = G_y = G_n^{(2)}$

We first discuss the 2:2 twisted chimera (cf. Fig. 15) in detail. In this case, two closed stripes of coherence are distributed uniformly on the torus. The local order parameter is written as

$$\tilde{Z}(x, y) = \sum_{m=1}^2 \{a_m \cos(mx) + b_m \sin(mx) + c_m \cos(my) + d_m \sin(my)\}, \quad (\text{C1})$$

with the coefficients satisfying the self-consistency relations

$$a_m = \langle \cos(mx') \exp(i\beta) \exp(i\Theta(x', y')) h(x', y') \rangle, \quad (\text{C2})$$

$$b_m = \langle \sin(mx') \exp(i\beta) \exp(i\Theta(x', y')) h(x', y') \rangle, \quad (\text{C3})$$

$$c_m = \langle \cos(my') \exp(i\beta) \exp(i\Theta(x', y')) h(x', y') \rangle, \quad (\text{C4})$$

$$d_m = \langle \sin(my') \exp(i\beta) \exp(i\Theta(x', y')) h(x', y') \rangle, \quad (\text{C5})$$

and h defined as in Eq. (11). From Figs. 15(b) and (c), we observe that the local order parameters have the symmetry

$$(x, y) \rightarrow (x + \delta, y + \delta) \implies (R, \Theta) \rightarrow (R, \Theta + 2\delta). \quad (\text{C6})$$

Thus

$$R(x + \delta, y + \delta) \exp(i\Theta(x + \delta, y + \delta)) = R(x, y) \exp(i\Theta(x, y) + 2i\delta), \quad (\text{C7})$$

which implies $a_1 = b_1 = c_1 = d_1 = 0$, $b_2 = ia_2$ and $d_2 = ic_2$. The symmetry

$$(x, y) \rightarrow (y, x) \implies (R, \Theta) \rightarrow (R, \Theta + \pi) \quad (\text{C8})$$

leads to the relations $a_2 = -c_2$ and $d_2 = -b_2$. Combining these results we obtain $\tilde{Z}(x, y) = a_2(\exp(2ix) - \exp(2iy))$. Translation symmetry in θ allows us to set $a_2 = R_0/2$, where R_0 is a positive real number. The final self-consistency equation is thus

$$R_0^2 = \exp(i\beta) \left\langle \Omega - \sqrt{\Omega^2 - R_0^2 \sin^2(x - y)} \right\rangle. \quad (\text{C9})$$

The 1:2 twisted chimera shown in Fig. 16 can be analyzed similarly. In this case, the local order parameter has the symmetry

$$(x, y) \rightarrow (x + 2\delta, y + \delta) \implies (R, \Theta) \rightarrow (R, \Theta + 2\delta), \quad (\text{C10})$$

implying that

$$R(x + 2\delta, y + \delta) \exp(i\Theta(x + 2\delta, y + \delta)) = R(x, y) \exp(i\Theta(x, y) + 2i\delta). \quad (\text{C11})$$

This condition is equivalent to $c_1 = d_1 = a_2 = b_2 = 0$, $b_1 = ia_1$ and $d_2 = ic_2$. The symmetry

$$(x, y) \rightarrow (2y, x/2) \implies (R, \Theta) \rightarrow (R, \Theta + \pi) \quad (\text{C12})$$

likewise yields $a_1 = -c_2$ and $b_1 = -d_2$ so that $\tilde{Z}(x, y) = a_1(\exp(ix) - \exp(2iy))$. With $a_1 = R_0/2$, we obtain the self-consistency equation

$$R_0^2 = \exp(i\beta) \left\langle \Omega - \sqrt{\Omega^2 - R_0^2 \sin^2(x/2 - y)} \right\rangle. \quad (\text{C13})$$

-
- [1] Y. Kuramoto and D. Battogtokh, *Coexistence of coherence and incoherence in nonlocally coupled phase oscillators*, Nonlinear Phenom. Complex Syst. **5**, 380 (2002).
 - [2] D. M. Abrams and S. H. Strogatz, *Chimera states for coupled oscillators*, Phys. Rev. Lett. **93** 174102 (2004).
 - [3] M. J. Panaggio and D. M. Abrams, *Chimera states: coexistence of coherence and incoherence in networks of coupled oscillators*, Nonlinearity **28**, R67 (2015).
 - [4] O. E. Omel'chenko, *Coherence-incoherence patterns in a ring of non-locally coupled phase oscillators*, Nonlinearity **26**, 2469 (2013).
 - [5] J. Xie, E. Knobloch, and H.-C. Kao, *Multicluster and traveling chimera states in nonlocal phase-coupled oscillators*, Phys. Rev. E **90**, 022919 (2014).
 - [6] Y. L. Maistrenko, A. Vasylenko, O. Sudakov, R. Levchenko, and V. L. Maistrenko, *Cascades of multiheaded chimera states for coupled phase oscillators*, Int. J. Bifurcation Chaos, **24**, 1440014 (2014).

- [7] E. Ott and T. M. Antonsen, *Low dimensional behavior of large systems of globally coupled oscillators*, *Chaos* **18**, 037113 (2008).
- [8] D. M. Abrams, R. Mirollo, S. H. Strogatz, and D. A. Wiley, *Solvable model for chimera states of coupled oscillators*, *Phys. Rev. Lett.* **101**, 084103 (2008).
- [9] Y. Kuramoto and S. Shima, *Rotating spirals without phase singularity in reaction-diffusion systems*, *Prog. Theor. Phys. Supp* **150**, 115 (2003).
- [10] S. Shima and Y. Kuramoto, *Rotating spiral waves with phase randomized core in nonlocally coupled oscillators*, *Phys. Rev. E* **69**, 036213 (2004).
- [11] O. E. Omel'chenko, M. Wolfrum, S. Yanchuk, Y. L. Maistrenko, and O. Sudakov, *Stationary patterns of coherence and incoherence in two-dimensional arrays of non-locally-coupled phase oscillators*, *Phys. Rev. E* **85**, 036210 (2012).
- [12] Y. Maistrenko, O. Sudakov, O. Osiv, and V. Maistrenko, *Chimera states in three dimensions*, *New J. Phys.* **17**, 073037 (2015).
- [13] E. A. Martens, C. R. Laing, and S. H. Strogatz, *Solvable model of spiral wave chimeras*, *Phys. Rev. Lett.* **104**, 044101 (2010).
- [14] P. Kim, T. Ko, H. Jeong, and H. Moon, *Pattern formation in a two-dimensional array of oscillators with phase-shifted coupling*, *Phys. Rev. E* **70**, 065201 (2004).
- [15] A. M. Hagerstrom, T. E. Murphy, R. Roy, P. Hövel, I. Omel'chenko, and E. Schöll, *Experimental observation of chimeras in coupled-map lattices*, *Nature Phys.* **8** 658 (2012).
- [16] M. J. Panaggio and D. M. Abrams, *Chimera states on a flat torus*, *Phys. Rev. Lett.* **110**, 094102 (2013).
- [17] M. Wolfrum, O. E. Omel'chenko, S. Yanchuk, and Y. L. Maistrenko, *Spectral properties of chimera states*, *Chaos* **21**, 013112 (2011).
- [18] C. R. Laing, *The dynamics of chimera states in heterogeneous Kuramoto networks*, *Physica D* **238**, 1569 (2009).
- [19] M. Dellnitz, M. Golubitsky, and M. Nicol, *Symmetry of attractors and the Karhunen–Loève decomposition*, in: *Trends and Perspectives in Applied Mathematics* (L. Sirovich, ed.), *Applied Mathematical Sciences* **100**, Springer-Verlag, New York (1994), pp. 73–108.
- [20] M. Field and M. Golubitsky, *Symmetry in Chaos*, 2nd ed., SIAM (2009).